Simulation of a detoxifying organ function: Focus on hemodynamics modeling and convection-reaction numerical simulation in microcirculatory networks

Noemie Boissier, Dirk Drasdo, Irene Vignon-Clementel

Received: xx | Journal Int. J. Num. Methods Biomed. Eng. | Online: Nov 2020
DOI: https://doi.org/10.1002/cnm.3422

ARTICLE TYPE

Simulation of a detoxifying organ function: focus on hemodynamics modeling and convection-reaction numerical simulation in microcirculatory networks.

Noemie Boissier[1,2,3] | **Dirk Drasdo**[1,2,3] | **Irene E. Vignon-Clementel***[1]

[1]Inria, Paris, France
[2]Laboratoire Jacques-Louis Lions, Sorbonne Université, CNRS, Université de Paris, Paris, France
[3]IfADo, Dortmund, Germany

Correspondence
*Corresponding Irene Vignon-Clementel, Centre de recherche Inria de Paris, 2 rue Simone Iff, 75012 Paris, France. Email: irene.vignon-clementel@inria.fr

Summary

When modelling a detoxifying organ function, an important component is the impact of flow on the metabolism of a compound of interest carried by the blood. We here study the effects of red blood cells (such as the Fahraeus-Lindqvist effect and plasma skimming) on blood flow in typical microcirculatory components such as tubes, bifurcations and entire networks, with particular emphasis on the liver as important representative of detoxifying organs. In one of the plasma skimming models, under certain conditions, oscillations between states are found and analysed in a methodical study to identify their causes and influencing parameters.

The flow solution obtained is then used to define the velocity at which a compound would be transported. A convection-reaction equation is studied to simulate the transport of a compound in blood and its uptake by the surrounding cells. Different types of signal sharpness have to be handled depending on the application to address different temporal compound concentration profiles. To permit executing the studied models numerically stable and accurate, we here extend existing transport schemes to handle converging bifurcations, and more generally multifurcations. We study the accuracy of different numerical schemes as well as the effect of reactions and of the network itself on the bolus shape. Even though this study is guided by applications in liver micro-architecture, the proposed methodology is general and can readily be applied to other capillary network geometries, hence to other organs or to bioengineered network designs.

KEYWORDS:
microcirculation; Farheus-Linqvist effect; plasma skimming; detoxifying organ; convection-reaction; numerical scheme for networks

1 | INTRODUCTION

Mathematical modeling of processes in physiological systems such as perfusion or function of organs is a field with growing interest largely because of its possible relevance for medical applications. Organs such as liver and kidney, detoxifying blood from potentially harmful compounds, are vital organs, whose functions have been widely studied in biology and medicine and need to be taken into account in drug development. In both organs, perfusion and detoxifying function are closely linked, and occur in repetitive anatomical and functional units at histological levels, the hepatic lobule in the liver, and the nephron in the kidney. At this level, the blood flows through networks of capillaries, which in contrast to large arteries and veins have so far only little been addressed. Novel imaging methods now permit 3D reconstruction of liver microarchitecture at a high level of detail[1], and transport as well as tissue reorganization processes occurring at microarchitectural level[2] raising the question how much detail is needed to perform realistic quantitative hemodynamics simulation at the level of capillary networks, and how certain model simplifications or modifications would affect characteristic observables. The aim of this paper is to establish a modeling framework for flow and transport in capillaries

including the temporal concentration profile, and certain uptake kinetics by parenchymal cells for compounds transported with the blood, as well as the numerical procedures to execute the models. This includes a step-wise study how different modeling hypotheses of the microcirculation affect perfusion and transport & exchange with the surrounding cells. Modeling hypotheses include dependencies on network architecture, different rheological effects, and different types of uptake kinetics (constant, linear, Michaelis-Menten-like) of cells from capillaries. For the rheological effects, models are compared to study their differences in hemodynamics starting with constant viscosity, adding the Fahraeus-Lindqvist-effect, and then plasma skimming, for which two existing models are considered. The model and parameter choices are complemented by a study of key numerical algorithms, especially for the transport part.

Experimental studies were carried out to characterize among others micro-vasculature [3,4,5], blood viscosity at this scale [6], or the movement within capillaries of erythrocytes, the red blood cells (RBCs) which are the main constituent of blood besides plasma [7,8,9,10]. A wide variety of models has been proposed to reproduce hemodynamics in single capillaries. Some focused on the interaction of RBCs with the endothelium (forming the capillary borders) with, for example, particle models [11,12,13]. Yet, applying this type of modeling approaches to a whole capillary network is computationally out of reach. Others focused on specific aspects of micro-circulation. Pries and Secomb [6,14], as well as Sharan and Popel [15] developed empirical laws to reproduce blood viscosity in the microcirculation. They include the Fahraeus-Lindqvist effect. This effect represents the hematocrit-and diameter-dependency of the viscosity of blood when flowing through a single vessel. Other models were proposed to mimic plasma skimming. This is the uneven distribution of cells at bifurcations (occuring at network branching points) [7]; the effect is also called bifurcation law, Zweifach-Fung effect law or phase separation law [8,16,17,18,19,20,21]. More extensive reviews on those aspects can be found in [22,23]. Others considered capillaries as a porous medium with a defined porosity [24,25]. Even if this approach permits to consider significant organ micro-architecture tissue samples, it however does not permit to account for the effect of RBCs on the flow, especially plasma skimming. Recently Possenti et al. [26] coupled the two approaches taking into account vessel tortuosity effect and coupling with interstitial flow. In all these studies, capillaries are considered far enough from the heart and thus, the temporal dependency of blood flow found in the main arteries due to heart beating can be neglected here. This is especially valid for liver that receives mostly venous blood. Some previous works proposed a dynamic approach, as in [27,28,29] to study specifically the effect of the RBCs on blood flow in a single or double bifurcation. Others coupled blood flow to vessel remodeling or angiogenesis, hence also studied the temporal evolution of blood flow, as in [30,31,32,33], but at a much larger time scale. In other studies on the influence of RBCs effects in microvascular networks, blood flow and hematocrit are considered stationary, still accounting for the different effects of RBCs on the flow [34,21,35,26]. Yet, none of these works focused on digestive organs micro-circulation in general, and on liver lobule hemodynamics in particular. These laws were compared in networks of rather larger radii than in a liver lobule [34,21,35] or on idealized networks [20,36]. When modeling an organ function, especially for digestive organs, the process of interest is often not blood flow per se, but the impact of the flow on the metabolism of a compound of interest carried by the blood. Depending on the time scales on which the process of interest happens, some aspects of the circulation need to be taken into account while others can be neglected. We here address the potential effect of erythrocytes on blood flow in kidney and liver as important representatives of digestive organs.

The flow solution obtained is then used to define the velocity at which the compound is transported. A convection-reaction equation (PDE) is studied to simulate the transport of a compound in blood and exchanges with the surrounding cells. Numerical methods to solve such equations in 1D in a single tube, in 2D and in 3D have been proposed [37]. However, very few studies investigated numerical methods to solve this equation in networks. Among them a few have been proposed in traffic flow in simple isolated bifurcations or multi-furcations [38], or water resources [39]. Drug transport in the liver has been the basis for pharmacokinetics studies in trees without exchanges in [40] or in a representative single tube connected to surrounding cells [41,42]. Different types of signals have to be handled: if a compound is ingested, its concentration input function in the liver will be smooth as the process lasts over several hours. However, when studying the metabolism of an injected bolus of drug or fluorescent compound, this signal can be extremely sharp and needs to be accurately simulated. A numerical scheme handling networks with successive multi-furcations is here proposed to simulate convection-reaction, with lower errors than first order schemes such as explicit upwind.

After describing the methods applied to study hemodynamics and solve the convection-reaction equation in capillary networks, hemodynamics results are presented in geometries from simple geometries to liver lobule networks, and the hypotheses or effects we believe important to properly model hemodynamics in these capillaries at steady state are detailed. Under certain conditions oscillations between states are found and analyzed in a methodical study to identify their causes and influencing parameters. Finally, results focused on the convection-reaction equation, show the accuracy of different numerical schemes as well as the effect of reactions and of the network itself on the bolus shape. This study orients along possible applications in liver micro-architecture but the proposed methodology is general and can readily be applied to other capillary network geometries, hence to other organs or to artificial network designs as e.g. bioengineered networks.

2 | METHODS

2.1 | Studied geometries

Blood enters capillaries that form a dense network through arterioles (and portal venules in the liver) and flows towards the venules connected to the vena cava. Before studying hemodynamics and advection-reaction in a capillary network, typical constitutive geometrical units of the network are first investigated: a single tube, a diverging and converging bifurcation (figure 1). Then, capillary networks are studied, focusing on liver micro-architecture. The liver parenchyma consists in a pattern of approximately hexagonal functional units, called liver lobules, in which arterial blood ($20-30\%$) enters through the hepatic artery (HA), and venous blood (70-80%) enters through the portal vein (PV). HA and PV together with the bile ducts that carry bile away from the liver lobule are defining the portal triads (PT). The capillary network is perfused by both HA and PV trees that join at the PT and we therefore consider a single blood inflow in liver capillaries incorporating both, thereafter labeled PT. Blood entering the lobule flows towards the central vein (CV), a venule of the hepatic vein tree located at the liver lobule center. Blood flow and transport are studied first in a simplified capillary network consisting in a diverging asymmetric tree generated with Zamir's law[43] followed by a converging one, and then in an image-based statistically representative liver lobule vascular network (figure 1 D)[44]. The *statistically representative* liver lobule has been constructed by sampling from 3D volume data sets from confocal laser scanning micrographs of liver tissue from mice. For the construction, the 3D volume data sets were parameterized by architectural parameters (e.g. sinusoidal radius, length between branches etc.[1]) and an artificial (the statistically representative) liver lobule has been generated by sampling from the distribution over the architectural parameters. As the field of view of the confocal images did not capture an entire liver lobule including its incoming and outgoing vessels, statistically representative lobules were the only way to construct an entire liver lobule.

In the following, any capillary network is described by a graph $G = \{N, E\}$, with N the set of nodes (intersections or graph nodes) and E the set of branches (or edges) modeled as straight cylinders. Let us define:

$$\begin{cases} N = \{i \text{ nodes }\} \\ E = \{(i,j) \in N^2 | \text{if a vessel connects nodes } i \text{ and } j\} \\ \delta_{i,j} = \begin{cases} 1 & \text{if } (i,j) \in E \\ 0 & \text{otherwise} \end{cases} \\ \Gamma(i) = \{j \in N | (i,j) \in E\} \quad \text{Neighbors of } i \quad \forall i \in N \\ Bc = \{i \in N | i \in (Inlet, Outlet)\} \\ Bc^- = \{i \in Bc | i \in Inlet\} \\ Bc^+ = \{i \in Bc | i \in Outlet\} \end{cases} \tag{1}$$

We have adopted the following notations for the network geometrical features:

- the radius is defined for each node as r_i but used only to compute the radius of edges
- the radius of each edge as $r_{i,j} = \frac{r_i + r_j}{2} \quad \forall (i,j) \in E$
- the length of an edge as $L_{i,j} \quad \forall (i,j) \in E$
- the cross section area of each edge as $A_{i,j} = \pi r_{i,j}^2 \quad \forall (i,j) \in E$
- the volume of each edge as $V_{i,j} = A_{i,j} L_{i,j} \quad \forall (i,j) \in E$
- the volume of a node i is the sum of each half edge's volume connected to it.
- $\alpha = \frac{r_{i,j1}}{r_{i,j2}}$ the radius asymmetry coefficient between two daugther branches $(i, j1)$ and $(i, j2)$ used in Zamir's asymmetric trees[43] applied to all intersections i.

The specific values are set depending on the studied cases and can be found in tables 1 for one tube, 2 for diverging bifurcations, 3 for networks.

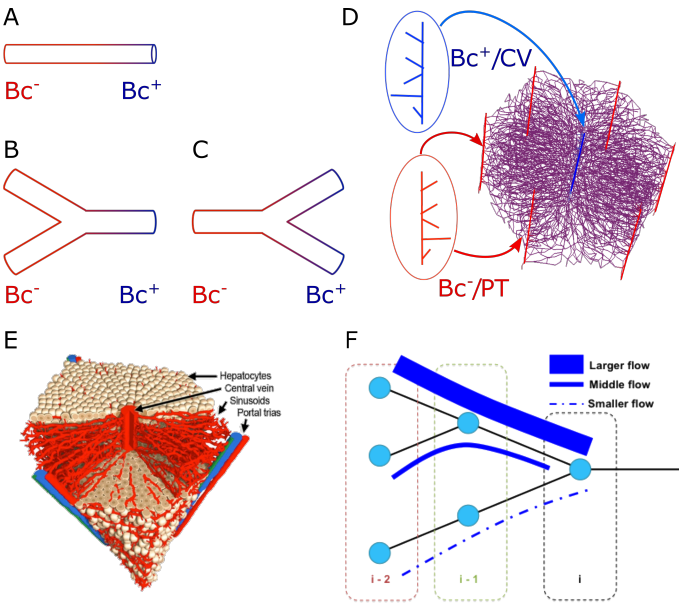

FIGURE 1 Geometries considered in this study; inlets Bc^- are in red, outlets Bc^+ in blue. A - one tube; B - a converging bifurcation with two inlets and a single outlet; C - a diverging bifurcation with one inlet and two outlets; D - a representative liver lobule graph with multiple inlets and outlets; the ovals show a zoom of how PTs and CVs are connected to several sinusoids; E - a 3D view of the representative lobule including hepatocytes[44]; F Schematic of the flow weights for intersection node i in the convection numerical scheme (26).

TABLE 1 Parameters and hemodynamics results in a single tube depending on the fluid effective viscosity with $\bar{v}$ the average flow velocity. In **bold**, the imposed fluid parameters. W stands for the viscosity law Eq. 47[14].

Radius (μm)	**Length** (μm)	**Viscosity**	**Resistance** (Pa.s/μm^3)	$\bar{\mathbf{v}}$ ($\mu m.s^{-1}$)	$\mathbf{\Delta P}$ (Pa)	**WSS** (Pa)
3.61	250	**Plasma**	$5.25\,10^{-3}$	1121.7	**241**	1.74
3.61	250	***Ex vivo***	$1.12 - 1.50\,10^{-2}$	$393 - 542$	**241**	1.74
3.61	250	$\mathbf{W(r, H_D)}$ $\mathbf{H_D = 0.442}$	$4.2\,10^{-2}$	140	**241**	1.74

TABLE 2 Description of diverging bifurcation types and parameters. r_i (resp. L_i) are the radius of the downstream branches $i \in 1, 2$ (resp. length), r_m (resp. L_m) the radius of the upstream mother branch (resp. length), Q_m the imposed total flow in the mother branch and $H_D(m)$ the imposed discharge hematocrit in the mother branch. The outlet pressure is 133Pa.

Case	**Organ**	$\mathbf{r_m}$ (μm)	$\mathbf{r_1}$ (μm)	$\mathbf{r_2}$ (μm)	$\mathbf{L_m}$ (μm)	$\mathbf{L_1}$ (μm)	$\mathbf{L_2}$ (μm)	$\mathbf{H_D(m)}$ (-)	$\mathbf{Q_m}$ ($\mu m^3.s^{-1}$)
1	Liver	3.61	2.32	4.9	16.57	16.57	16.57	**0.442**	**5683**
2	Liver	3.61	3.61	3.61	16.57	4.99	28.15	**0.442**	**5683**
3	Liver	3.61	3.61	3.61	16.57	4.99	28.15	**0.34**	**5683**
4	Liver	3.61	3.61	3.61	16.57	4.99	28.15	**0.442**	**8065**
5	Liver	3.61	3.61	3.61	16.57	4.99	28.15	**0.442**	**3316**
6	Liver	3.61	2.32	4.9	16.57	16.57	16.57	**0.442**	**3316**
7	Liver	3.61	2.32	4.9	125	177	177	**0.442**	**5683**
8	Kidney	4.4	3	5.8	26.3	26.3	26.3	**0.442**	**103396**
9	Kidney	4.4	4.4	4.4	26.3	1.4	51.2	**0.442**	**103396**
10	Kidney	4.4	3	5.8	26.3	26.3	26.3	**0.442**	**237203**
11	Kidney	4.4	4.4	4.4	26.3	1.4	51.2	**0.442**	**237203**

TABLE 3 Liver lobule networks parameters and hemodynamics results. In **bold**, the imposed parameters conditions. The outlet pressure is 133Pa. W stands for the viscosity law Eq. 47[14] without plasma skimming included. Asymmetric trees have a constant branch length L=16.57μm.

Name (-)	**Radius $\pm$ SD** (μm)	**Viscosity** (-)	**Resistance** (Pa.s/μm^3)	$\bar{\mathbf{v}}$ ($\mu m.s^{-1}$)	$\mathbf{\Delta P}$ (Pa)	**WSS** (Pa)
Asymmetric tree	1.54 - 10	$\mathbf{W(r, H_D)}$	figure 4 B	at inlet: $\mathbf{138.8}$	-	-
Constant r lobule (CLL)	3.61	$\mathbf{W(r, H_D)}$	$2.0\,10^{-4}$	79.7	$\mathbf{282}$	figure 15
Healthy lobule (HLL)	3.61 ± 1.19	$\mathbf{W(r, H_D)}$	$2.7\,10^{-4}$	61.1	$\mathbf{282}$	figure 15
Dilated network (DLL)	3.61 ± 1.19	$\mathbf{W(r, H_D)}$	$2.0\,10^{-4}$	73.4	$\mathbf{282}$	figure 15
in Peri-Central DLL	4.33 ± 1.19					

TABLE 4 Literature values of capillary radii, flows and pressures in two blood filtering organs: kidney and liver.

Radius in μm	**Organ**	**Animal**	**Technique**	**Ref**
2.5	Liver	Mouse	Staining	Theruvath 2006[45]
3.32 ± 0.20	Liver	Mouse	Intra vital 2d	Sidler 2008[46]
2.95 ± 0.05	Peri-portal liver	Mouse	High resol in vivo imaging	MacPhee 1995[9]
3.65 ± 0.05	Mid-zonal liver	Mouse	High resol in vivo imaging	MacPhee 1995[9]
6.85 ± 0.7	Peri-central liver	Mouse	Synchroton Radiation MicroComputed Tomography	Yoon 2013[47]
4.4 ± 1.2	Peri-portal liver	Mouse	Synchroton Radiation MicroComputed Tomography	Yoon 2013[47]
4.25 ± 0.05	Liver	Mouse	Intra vital 3d	Vollmar 1998[48]
4.6	Liver	Mouse	Electron Microscopy	Dill 2012[49]
2.15 ± 0.17	Liver	Mouse	Intra vital 2d	Chen 2014[50]
2.185 ± 0.03	Liver	Mouse	Intra vital column of plasma (underestimates diameter)	Vanheule 2008[51]
$2.85 - 3.05$	Liver	Mouse	Electron Microscopy	Eguchi 1991[52]
4.25 ± 1.32	Liver	Mouse	Staining 2D bright field	Aidoo 2012[53]
3.85 ± 1.05	Kidney	Rat	Electron Microscopy	Adamczak et al 2004[54]
4.96 ± 1.77	Kidney	Rat	3D staining	Remuzzi et al 1992[55]
Velocity value $\mu m.s^{-1}$	**Organ**	**Animal**	**Technique**	**Reference**
$128 \pm 26 - 149 \pm 49$	Liver	Mouse		Theruvath 2006[45]
209.3 ± 33.16	Liver	Mouse	Intra vital	Sidler 2008[46]
69.2 ± 4.5	Liver	Mouse	Video flying-spot	MacPhee 1995[9]
250 ± 3	Liver	Rat	Video flying-spot	Komatsu et al. 1990[56]
60	Liver	Mouse	Intra vital	Rocca 2011[57]
$1.7e3 \pm 2.2e3$	Kidney	Rat	Model	Remuzzi et al 1992[55]
$\triangle$ P in Pa	**Organ**	**Animal**	**Technique**	**Ref**
133	Liver	Rabbits		Maass-Moreno 1997[58]
26.6	Liver	Rats	Model Lower Left Lobe	Debbaut 2012[24]
119.7	Liver	Rats	Model Lower Middle Lobe	Debbaut 2012[24]
392.266	Liver	Rats		Shibayama and Nakata 1985[59]
294.1995	Liver	Rat		Nakata 1960[60]
539.36575	Liver	Rat		Nakata 1960[60]
4921	Kidney	Rat	Micropuncture	Remuzzi et al 1992[55]

2.2 | Hemodynamics model

In the micro-vasculature, flow pulsatility can be neglected and blood flow is assumed to be stationary. We approximate capillaries by non-leaky rigid cylinders, and blood to be an incompressible viscous fluid. We thereby neglect that liver sinusoids are fenestrated[9] with an approximately $0.5\mu m$ wide, extracellular matrix and non-parenchyma cells filled space (Disse space) between sinusoidal endothelial cells and hepatocytes[61], as the dense extracellular matrix drags down flow speed. The Reynold's number is below 10^{-3} and blood flow within each edge is modelled by Poiseuille law following the motivation and hypotheses of Pries and Secomb[23], while mass conservation is ensured at each node of G. Let us thus define:

- P_i the pressure at node $i \in N$
- $Q_{i,j}$ the flow going through edge $(i,j) \in E$
- $\Gamma^+(i) = \{j \in \Gamma(i) | P_j \leq P_i\}$
- $\Gamma^-(i) = \{j \in \Gamma(i) | P_i \leq P_j\}$
- $Q_i = \sum_{j \in \Gamma^+(i)} Q_{i,j}$ the total inflow going in node i
- $\eta_{i,j} \quad (i,j) \in E$ the apparent viscosity of blood in the edge
- $R_{i,j} = \frac{8\eta_{i,j} L_{i,j}}{\pi r_{i,j}^4} \quad \forall (i,j) \in E$ the resistance of the edge

Poiseuille law thus reads $P_i - P_j = R_{i,j} Q_{i,j}$. This description is thus the one of a fluid, whose effective or apparent Newtonian viscosity in each capillary takes into account non-Newtonian effects[23]. Moreover, the transported compounds that are then taken up by parenchyma cells have small sizes compared to the capillary diameter, therefore are assumed to have no influence on the simulated blood flow.

Closing conditions Q_{Bc} and P_{Bc}, called thereafter boundary conditions, of either flow or pressure are set at the network's inlets and a pressure is imposed at its outlets, e.g:

$$\begin{aligned} Q_i &= \frac{Q_{lobule}}{\textbf{Card(}Bc^+\textbf{)}} \quad \forall i \in Bc^- \\ P_i &= P_{imposed} \quad \forall i \in Bc^+ \end{aligned} \tag{2}$$

with **Card(X)** the number of elements of X. Boundary conditions are set such that the resulting average flow velocity is within physiological ranges, with a pressure difference also within physiological ranges, that are reported in table 4. From now on, for a node quantity X_i (or $X(i)$) or an edge quantity $X_{i,j}$ (or $X(i,j)$), X will represent the corresponding vector of the relevant size.

Blood is a mixture of plasma with cells, mainly erythrocytes (RBCs). Having a diameter of the order of magnitude of the capillaries' diameter, they are expected to have an effect on blood flow. Hematocrit is a measure of RBCs concentration in blood. The discharge hematocrit $H_D(i,j)$ is defined on each edge; it represents the ratio of erythrocyte flow and blood flow, entering or leaving the tube[23].

First, to account for the effect of RBCs on blood apparent viscosity, the Fahraeus-Linqvist effect, Pries and Secomb[14] proposed an empirical law that links the vessel radius $r_{i,j}$ and discharge hematocrit $H_D(i,j)$ to the blood apparent viscosity and is referred to as $W(r_{i,j}, H_D(i,j), \eta_{plasma})$ with $\eta_{plasma} = 1.31mPa.s$ defined in Eq. 47.

Then, at bifurcations, the distribution of erythrocytes in downstream branches can deviate from blood flow distribution. This phenomenon, defined as plasma skimming, has been observed first by Krogh in 1921[7]. Since then, several models have been proposed to predict the distribution of red blood cells in the downstream branches (i.e. m, j such that $j \in \Gamma^+(m)$) of a diverging node m based on the fractional blood flow $FQ^B(m,j)$ and the fractional erythrocytes flow $FQ^E_{m,j}$ defined as:

$$FQ^B(m,j) = \frac{Q_{m,j}}{Q_m} \; ; \; FQ^E(m,j) = \frac{Q_{m,j} H_D(m,j)}{Q_m H_D(m)} \tag{3}$$

with Q_m, the inflow crossing the node m, and

$$H_D(m) = \frac{\sum_{j \in \Gamma^-(m)} |Q_{m,j}| H_D(m,j)}{Q_m} \tag{4}$$

that corresponds to the weighted average of the discharge hematocrit in the upstream branches of the intersection. Thus, knowing $FQ^E(m,j)$, one can compute $H_D(m,j) = \frac{FQ^E(m,j)}{FQ^B(m,j)} H_D(m)$, thereby defining the plasma skimming function F in the implicit equation $H_D(m,j) = F(Q, H_D, r)(m,j)$. Pries and Secomb.[19] proposed an empirical non-linear law for $FQ^E_{m,j}$ that takes into account the downstream branches radii asymmetry as well as the individual branches radii. This function is the most widely applied to predict discharge hematocrit at bifurcations and permits to reproduce extreme cases for which all the RBCs flow into only one of the two daughter branches ($Card(\Gamma^+) = 2$, $d1 = (m,1), d2 = (m,2)$). It reads:

$$FQ^E_{d1} = \begin{cases} 0 \quad \text{if } FQ^B_{d1} < X_0 \\ [1 + \exp(A - B \log(\frac{FQ^B_{d1} - X_0}{1 - FQ^B_{d1} - X_0})]^{-1} \\ \quad \text{if } X_0 \leq FQ^B_{d1} \leq 1 - X_0 \\ 1 \quad \text{if } FQ^B_{d1} > 1 - X_0 \end{cases} \tag{5}$$

with

$$\begin{cases} X_0 = \dfrac{0.4}{2r_m} \\ A = \dfrac{-6.96}{2r_m} \log(\dfrac{r_{d2}}{r_{d1}}) \\ B = 1 + 6.98 \left(\dfrac{1 - H_D(m)}{2r_m} \right) \end{cases} \tag{6}$$

when $r_{d1} \leq r_{d2}$, and with r_m the radius of the mother branch. To ensure mass conservation, FQ^E_{d2} is set as follows:

$$FQ^E_{d2} = 1 - FQ^E_{d1} \tag{7}$$

Recently, Gould and Linninger[21] proposed an empirical plasma skimming law, linear in H_D, that can handle multi-furcations ($Card(\Gamma^+) \geq$

2). It reads for $j \in \Gamma^+(m)$:

$$FQ^E_{m,j} = \frac{Q_{m,j}\theta_{m,j}}{\sum_{(m,i)\in E|i\in\Gamma^+(m)} Q_{m,i}\theta_{m,i}}$$
$$\theta_{m,j} = \left(\frac{A_{m,j}}{A_m}\right)^{\frac{1}{M}} \quad (8)$$

The parameter values $M = 1.13$ for a single bifurcation and $M = 5.25$ for an entire network have been found to fit experimental data. Figure 9(B) shows the fractional erythrocytes flow for the three laws considered here.

The combined models thus lead to the following system of equations:

$$\begin{cases} H_D(i,j) = F(Q, H_D, r)(i,j) \\ \eta_{i,j} = W(r_{i,j}, H_D(i,j)) \quad \forall (i,j) \in E \\ \sum_j \frac{P_i - P_j}{R_{i,j}(\eta_{i,j}, r_{i,j})} = 0 \quad \forall i \in N \setminus Bc \\ P_i = P_{bc,i} \quad \forall i \in Bc^+ \\ \forall i \in Bc^-, \begin{cases} P_i = P_{bc,i} \text{ if pressure BC} \\ \sum_j \frac{P_i - P_j}{R_{i,j}(\eta_{i,j}, r_{i,j})} = Q_{bc,i} \text{ if flow BC} \end{cases} \end{cases} \quad (9)$$

with $F(Q, H_D, r)$ the applied plasma skimming law, $W(r, H_D)$ the viscosity law.

This system of coupled equations is solved as follows. In all cases, discharge hematocrit is initialized at the baseline value of $H_D^{baseline} = 0.442$, which is the value in the larger feeding vessels (here PV)[14]. Unless viscosity is set to a constant value, the non-Newtonian effect of RBCs on apparent viscosity enters indirectly in the computation of the branch resistance through W. Flow and pressure boundary conditions are set. The pressure system (the last 4 equations of 9) is a sparse linear system of size (Card$(N)\times$Card(N)). Under physiological conditions, the matrix conditioning number for the norm $\mathcal{L}_\infty$ is close to 10^6. A Jacobi preconditionner is therefore applied and the system is solved by a bi-conjugated gradient stabilized algorithm (BiCGSTAB, from van der Vorst[62]). Once the pressure field is computed, the flow in each branch is updated with Poiseuille law. When plasma skimming is considered, $H_D(i) = H_D^{baseline} \forall i \in Bc^-$, and H_D is computed through F. In this case, algorithm 1 summarizes the different steps of the resulting coupled nonlinear system, solved with a fixed-point algorithm which converging criteria is set as:

$$Crit = \max_{(i,j)\in E} \left(Q^{it+1}_{i,j} - Q^{it}_{i,j}\right) \quad (10)$$

with it the number of iterations. The stopping condition is set to either $Crit < \epsilon$ or $it > N_{maxIt}$. In a bifurcation, $\epsilon = 10^{-6}\mu m^3.s^{-1}$ and $N_{maxIt} = 2000$. Because the network consists of many segments and therefore shows a high number of branches in which the flow is low, $\epsilon = 10^{-2}\mu m^3.s^{-1}$ and $N_{maxIt} = 1200$. In both cases, the average flow values are around $10^3\mu m^3.s^{-1}$, hence significantly higher than ϵ. Contrarily to the Gould & Linninger law which is linear in H_D and thus results in a linear system to solve for H_D, the plasma skimming law proposed by Pries and Secomb is nonlinear in H_D (and will be referred to as nonlinear law in the following) and requires an internal loop updating the discharge hematocrit depending on the flow. The convergence criterion of this loop is computed the same way as $Crit$ but for discharge hematocrit and the stopping condition is set at 10^{-5} independently of the geometry.

Algorithm 1 Hemodynamics computation algorithm

procedure Hemodynamics computation([Q,P] = HemoComputation(Q_{Bc}, P_{Bc}, H_D))
  set Q_{Bc}, P_{Bc} and initialize H_D
  Crit = ∞
  it = 0
  [Q,P] = ComputeFlow(Q_{Bc}, P_{Bc}, H_D)
  while $Crit \geq \epsilon \,\&\, it \leq 1200$ **do**
    Tag Γ^- and Γ^+ for each node m.
    Q^* = Q
    H_D^* = ComputeHD(Q^*) (if nonlinear plasma skimming law: through fixed-point)
    [Q,P] = ComputeFlow(Q_{Bc}, P_{Bc}, H_D^*)
    Crit = $\max|Q^* - Q|$
    it = it + 1
  end while
  return [Q,P]
end procedure

The applied parameters and boundary conditions are detailed in tables 1, 2, 3 and 4.

2.3 | Substance spread model

Hemodynamics modeling in the microarchitecture of detoxifying organs is the basis to explain or predict the effect of drugs or diseases on the organ function. The blood flow model detailed above provides a blood flow velocity field entering in the simulation of transport and reaction of a drug, metabolite or any other substance in the vascular network.

2.3.1 | Modeling convection-reaction in detoxifying organ micro-architecture

In this work, diffusion is neglected in both the longitudinal and axial directions as the characteristic time for a substance of interest to diffuse along a segment of a cell length is significantly higher than the characteristic time of convection: for taurocholate, a liver bile salt, it reaches $4.2s$ for diffusion vs. $0.18s$ for an average blood velocity of $138.8\mu m.s^{-1}$ and diffusion constant of $D = 150\mu m^2.s^{-1}$[63]. The considered convection-reaction equation for the substance blood concentration c over time t therefore is:

$$\begin{cases} \frac{\partial c}{\partial t} + \nabla \cdot (vc) = -f \quad \forall t \in T \\ c(Bc^-, t) = g(t) \quad \forall t \in T \end{cases} \quad (11)$$

in domain Ω. T is the time interval, v the flow velocity from the hemodynamics model in section 2.2 and f a reaction-like term mimicking the exchange between blood and surrounding cells. Because of the network structure of the domain and the flow considered unidirectional, axisymmetric and developed in each vessel, this problem is considered essentially $1D$ along each vessel (edge) and locally $3D$ at intersections, that are treated as detailed in section 2.3.2.

Several types of exchanges along each vessel exist between cells and blood, among them passive diffusion or active uptake of substances that can be saturated. This study focuses on the active uptake of the transported substance from the blood by parenchyma cells by a Michaelis-Menten kinetics [64] as showcase, leading to:

$$f(\cdot,t) = \frac{v_{r,max}c(\cdot,t)}{K_{r,m}+c(\cdot,t)} \tag{12}$$

with

- a linear regime in $c(\cdot,t)$ when $c(\cdot,t)$ is much lower than the so-called Michaelis constant $K_{r,m}$, resulting in:

$$f(\cdot,t) \sim \frac{v_{r,max}}{K_{r,m}}c(\cdot,t) \tag{13}$$

- a saturated regime independent of $c(\cdot,t)$, when $c(\cdot,t) \gg K_{r,m}$, resulting in:

$$f(\cdot,t) \sim v_{r,max}\text{(hence called maximum rate)} \tag{14}$$

2.3.2 | Numerical methods

Most liver functions are linked to blood detoxification of substances that have been ingested and digested. The corresponding input concentration profiles span over several hours, hence the model needs to simulate convection-reaction equations over the same time. However, for some drugs or fluorescent markers, the focus is on the first pass effect which requires an accurate simulation of the convection equation over a short period of time. Thus, the numerical scheme has to be versatile enough to adapt to both situations, which could be of interest for the same compound. Moreover, to reproduce the studied liver function, this convection-reaction equation is then coupled to a system of ODEs accounting for the compound metabolism by cells and implemented in each one of them inside the geometry. Finally, to calibrate parameters by minimizing the error of the simulated concentrations with experimental data, such simulations will be run a significant number of times. Therefore, the choice of numerical scheme for the convection-reaction equation should avoid too high computational times.

General discretization

Many numerical schemes exist to solve equation (11), [37,65,38]. According to a classical choice to simulate convection-reaction in $1D$, a finite volume scheme is used. The integration of equation (11) over a network volume (a vessel piece or a junction, which lateral walls are the ones of the vessels) therefore reads:

$$\int_{\Omega_i} \frac{\partial c}{\partial t} d\Omega = -\int_{\Omega_i} \nabla\cdot(vc)d\Omega - \int_{\Omega_i} \frac{v_{r,max}c}{K_{r,m}+c}d\Omega \tag{15}$$

with Ω_i being the numerical cell associated with node i. Applying the Green-Ostrogradski formula, and assuming the fluxes perpendicular to the vessels' walls are null coherently with the hypothesis of non-slip flow condition, the discretized equations read

$$\begin{aligned}
&\int_{\Omega_i} \frac{v_{r,max}c}{K_{r,m}+c}d\Omega \sim \frac{v_{r,max}\bar{c}_i}{K_{r,m}+\bar{c}_i}V_i,\\
&\frac{\partial \bar{c}_i V_i}{\partial t} \sim \sum_{j\in\Gamma^-(i)} \int_{\sigma_i^-} vcd\sigma - \sum_{j\in\Gamma^+(i)} \int_{\sigma_i^+} vcd\sigma - \frac{v_{r,max}\bar{c}_i}{K_{r,m}+\bar{c}_i}V_i,\\
&\frac{dU_i}{dt} \sim F_{i-\frac{1}{2}} - F_{i+\frac{1}{2}} - \frac{V_{r,max,i}U_i/V_i}{K_m+U_i/V_i},
\end{aligned} \tag{16}$$

with

$$\begin{cases}
F_{i-\frac{1}{2}} = \sum_{j\in\Gamma^-(i)} \int_{\sigma_i^-} vcd\sigma\\
F_{i+\frac{1}{2}} = \sum_{j\in\Gamma^+(i)} \int_{\sigma_i^+} vcd\sigma
\end{cases} \tag{17}$$

with $V_{r,max,i} = V_i v_{r,max}$ and with V_i the volume of the numerical cell i (that corresponds to the node i), v the blood velocity, $\bar{c}_i$ the average concentration over the numerical cell i, U_i the corresponding amount of substance. To solve this system, an explicit scheme is chosen for both computational time and numerical diffusion reduction reasons, giving:

$$U_i^{n+1} - U_i^n = \Delta t \left(F_{i-\frac{1}{2}}^n - F_{i+\frac{1}{2}}^n - \frac{V_{r,max,i}U_i^n/V_i}{K_m+U_i^n/V_i} \right) \quad \forall n \in T \tag{18}$$

with $T = \{n\}$ studied time points.

Scheme first order in space

An explicit upwind scheme first order in space and time is considered, reading, for a multi-furcation or intersection:

$$\begin{aligned}
F_{i-\frac{1}{2}}^n &= \Delta t \left(\sum_{j\in\Gamma^-(i)} \int_{\sigma_{j,i}^-} \bar{c}_j^n v_{j,i} d\sigma \right)\\
&= \Delta t \left(\sum_{j\in\Gamma^-(i)} \frac{U_j^n}{V_j} Q_{j,i} \right)\\
F_{i+\frac{1}{2}}^n &= \Delta t \left(\sum_{j\in\Gamma^+(i)} \int_{\sigma_{i,j}^+} \bar{c}_i^n v_{i,j} d\sigma \right)\\
&= \Delta t \left(\frac{U_i^n}{V_i} \sum_{j\in\Gamma^+(i)} Q_{i,j} \right)\\
&\forall n \in T \quad \forall i \in N
\end{aligned} \tag{19}$$

with $\sigma_{i,j}^+$ (resp. $\sigma_{i,j}^-$) the boundary between i and $j \in \Gamma^+$ (resp. $j \in \Gamma^-$).

To ensure stability, the time step Δt is set such that the CFL (Courant Friedrichs Lewy) condition is always respected, leading to, for an intersection:

$$\Delta t = \min_{i\in N} \frac{V_i}{Q_i + V_{r,max,i}/K_{r,m}} \tag{20}$$

Approximation of the second order in space

If in the micro-vasculature the injected bolus is smoothed by the systemic and pulmonary circulation, the arterial profile of some drugs or markers remain sharp (figure 8B). To avoid numerical diffusion and oscillations introduced by a linear discretization of space that leads

to a second order scheme [37], flux limiters are introduced leading to a nonlinear higher order scheme.

Flux limiters or slope limiters consist in a nonlinear discretization of the convection equation. This is a solution to reduce the numerical diffusion while avoiding oscillations. In case of a single tube, as detailed in [37], the numerical fluxes are:

$$\begin{aligned} F^n_{i-\frac{1}{2}} &= \Delta t \left(Q_{i-1,i} \frac{U^n_{i-1}}{V_{i-1}} + \frac{1}{2} Q_{i-1,i} (1 - \Delta t \frac{Q_{i-1,i}}{V_{i-1}}) \right. \\ &\quad \left. \phi \left(\frac{U^n_{i-1}/V_{i-1} - U^n_{i-2}/V_{i-2}}{U^n_i/V_i - U^n_{i-1}/V_{i-1}} \right) \left(\frac{U^n_i}{V_i} - \frac{U^n_{i-1}}{V_{i-1}} \right) \right) \\ F^n_{i+\frac{1}{2}} &= \Delta t \left(\frac{U^n_i Q_{i,i+1}}{V_i} + \frac{1}{2} Q_{i,i+1} (1 - \Delta t \frac{Q_{i,i+1}}{V_i}) \right. \\ &\quad \left. \phi \left(\frac{U^n_i/V_i - U^n_{i-1}/V_{i-1}}{U^n_{i+1}/V_{i+1} - U^n_i/V_i} \right) \left(\frac{U^n_{i+1}}{V_{i+1}} - \frac{U^n_i}{V_i} \right) \right) \end{aligned} \quad (21)$$

$\forall n \in T \quad \forall i \in N$

with, for each node i:

- the nodes $i+1$ correspond to the set of nodes $\Gamma^+(i)$
- the nodes $i-1$ correspond to the set of nodes $\Gamma^-(i)$
- the nodes $i-2$ correspond to the set of nodes $\Gamma^{--}(i)$

$\phi(\cdot)$ is the slope or converginger function. Many of those functions exist but we choose to focus on the most commonly applied ones:

- the minmod limiter, from Roe in [66] with

$$\phi(r) = \max(0, \min(1, r)) \quad (22)$$

- the superbee limiter, from Roe in [66] with

$$\phi(r) = \max(0, \min(2r, 1), \min(r, 2)) \quad (23)$$

- the MC limiter, from Van Leer in [67] with

$$\phi(r) = \max(0, \min(2r, 0.5(1 + r), 2)) \quad (24)$$

- the Van Leer limiter, from Van Leer in [68] with

$$\phi(r) = \frac{r + |r|}{1 + |r|} \quad (25)$$

This scheme is here extended to a network of intersections connected by segments. All possible fluxes are computed as described above. $F_{i-1/2}$ and $F_{i+1/2}$ are then the weighted sum of those fluxes. The weight applied for each flux is the ratio of branches flow over the sum of all flows, giving the numerical scheme described in system (26) (figure 1F).

$$\begin{aligned} F^n_{i-\frac{1}{2}} &= \Delta t \left(\sum_{j \in \Gamma^-(i)} \frac{Q_{j,i} U^n_j}{V_j} + \sum_{j \in \Gamma^-(i)} \sum_{p \in \Gamma^-(j)} \frac{Q_{p,j}}{Q_j} \right. \\ &\quad \left. \frac{1}{2} Q_{j,i} (1 - \Delta t \frac{Q_{j,i}}{V_j}) \phi \left(\frac{U^n_j/V_j - U^n_p/V_p}{U^n_i/V_i - U^n_j/V_j} \right) \left(\frac{U^n_i}{V_i} - \frac{U^n_j}{V_j} \right) \right) \\ F^n_{i+\frac{1}{2}} &= \Delta t \left(\frac{U^n_i \sum_{j \in \Gamma^+(i)} Q_{i,j}}{V_i} + \sum_{j \in \Gamma^-(i)} \sum_{k \in \Gamma^+(i)} \frac{Q_{j,i}}{Q_i} \right. \\ &\quad \left. \frac{1}{2} Q_{i,k} (1 - \Delta t \frac{Q_{i,k}}{V_i}) \phi \left(\frac{U^n_i/V_i - U^n_j/V_j}{U^n_k/V_k - U^n_i/V_i} \right) \left(\frac{U^n_k}{V_k} - \frac{U^n_i}{V_i} \right) \right) \end{aligned} \quad (26)$$

$\forall n \in T \quad \forall i \in N$

By construction, these fluxes respect mass conservation.

Boundary conditions

Boundary conditions of equation (11) are handled as described by Leveque in [37]:

- Ghost cells are introduced for inlet nodes $i \in Bc^-$ with:

$$\begin{aligned} U^n_{i-1}/V_{i-1} &= g(n\Delta t + \frac{V_i}{2 \sum_{j \in \Gamma^+(i)} Q_{i,j}}) \\ U^n_{i-2}/V_{i-2} &= g(n\Delta t + \frac{3V_i}{2 \sum_{j \in \Gamma^+(i)} Q_{i,j}}) \\ &\forall n \in T \quad \forall i \in Bc^- \end{aligned} \quad (27)$$

  with $g(t)$ the input function (equation (16)),

- at the outlet, for stability reasons [37], a first order scheme is considered for the leaving numerical flux:

$$F^n_{i+\frac{1}{2}} = \sum_{j \in \Gamma^-(i)} \frac{Q_{j,i}}{V_i} U^n_i \quad (28)$$

$\forall n \in T \quad \forall i \in Bc^+$

2.4 | Quantifying dispersion introduced by a network

The study of a bolus dispersion in an organ vasculature is a subject by itself. It has several applications, among them determining the presence of a tumor or quantifying its size, density of vasculature. To investigate how liver micro-vasculature disperses an injected bolus, several indicators have been introduced such as the mean transit time [69]:

$$\bar{T} = \int_{t=0}^{\infty} R(t) dt \quad (29)$$

with $R(t)$ the residue function of the network:

$$R(t) = 1 - \frac{\int_0^t C_{out}(t') dt'}{\int_0^\infty C_{out}(t') dt'}. \quad (30)$$

The mean transit time represents the mean time a particle entering the capillary network spends in it. It can be related to the transfer function of the network, computed as:

$$h(t) = -\frac{dR(t)}{dt} \quad (31)$$

To compute $h(t)$, we chose to consider only convection to evaluate the impact of the network alone on the computed dispersion.

Hence, we propose to use a *point wise* approach to compute the convection solution, that avoids introducing numerical diffusion. It consists in defining how concentration is transported through a bifurcation and using the analytic solution in each edge from the one known in a tube:

$$\begin{cases} c_i(t) = \sum_{j \in \Gamma^-(i)} c_j(t - \frac{L_{j,i}}{v_{j,i}}) \frac{Q_{j,i}}{Q_i} & \forall i \in \text{converging inter.} \\ c_j(t) = c_i(t - \frac{L_{i,j}}{v_{i,j}}) & \forall j \in \Gamma^+(i); \forall i \in \text{diverging inter.} \end{cases} \quad (32)$$

Moreover, we choose a time interval and input bolus such that:

$$\exists t_0 \in T | \forall t \geq t_0 \quad C_{out}(t) = 0 \quad (33)$$

3 | RESULTS AND DISCUSSION

Hemodynamic patterns in unit geometries, first, and then in capillary networks representing the liver micro-architecture with parameters

detailed in tables 1, 2, 3 and 4 are first described. Building on the computed velocity, convection-reaction is then studied.

3.1 | Hemodynamics results

3.1.1 | Single vessel case

A representative vessel of radius $r = 3.61\mu m$ and length $L = 250\mu m$, the approximate liver lobule radius, is considered first as an idealization of a sinusoid linking PT and CV. Both inlet and outlet pressures are set such that the pressure difference is within physiological ranges, $\Delta P = 241Pa$. When blood is modelled as plasma only, the obtained velocity is nearly ten fold higher than the average measured velocities (table 1). Setting blood viscosity to constant measured values *ex vivo*, of $3 - 4\,10^{-3}Pa.s$ [70], leads to velocities between $5.2\,10^{2}\mu m.s^{-1}$ and $3.9\,10^{2}\mu m.s^{-1}$, which is also significantly higher than measured values. RBCs increase the apparent fluid viscosity, therefore reduce the simulated average velocity for a given pressure difference boundary condition. Finally, when including W the obtained average velocities are close to those measured (table 4). Therefore, both blood nature deviation from plasma and the Fahraeus-Linqvist effect influence on viscosity need to be included.

3.1.2 | Effect of plasma skimming on a unit bifurcation

From now on, the Fahraeus-Lindqvist effect W is included in the hemodynamics model. To determine the effect of plasma skimming on the simulated hemodynamics, the impact of the two laws in section 2.2 is studied in diverging bifurcations with flow boundary conditions at the inlet and a pressure set at the outlet (figure 1 C, table 2). The 'linear law' will from now on refer to the one from Gould & Linninger, whereas the 'non-linear law' will refer to the one of Pries & Secomb.

Plasma skimming homogenizes the simulated blood flow

Consider the case of diverging bifurcations where there is a radius change between mother and daughters, and where daughters radii are different. For both laws (linear and nonlinear) blood flow rates in the daughter branches are closer to each other than when no plasma skimming is taken into account (figure 2 B, circle cases). Both laws increase flow in the branch with the smallest diameter by predicting a decrease of the discharge hematocrit, which for the nonlinear law can go down to zero, corresponding to an erythrocytes' free branch. This result is coherent with numerical observations from Schmid et.al. [36]. By contrast, for diverging bifurcations where only lengths vary but not diameter, by design only the nonlinear exhibits differences with the other ones: here too it tends to homogenize flow rates between the two uneven daughter branches (figure 2 B, - cases).

The linear model effect can be neglected compared to the nonlinear one

It appears that the nonlinear law and the linear law with $M = 1.13$ have a stronger effect on the simulated flow than the linear law with $M = 5.25$ (figure 2 A). When only the downstream branches' length differ (cases 2 to 5), an even distribution of discharge hematocrit is predicted with the linear law, independently of the flow distribution asymmetry (figure 2 B). The nonlinear law, on the contrary, predicts different discharge hematocrits in the two downstream branches.

Study of the different states as a function of geometry and hematocrit H_D

To better understand the effect of parameters on the solution, the daughter branches radii are varied within physiological ranges for a given radius of the mother branch. Blood flow including the nonlinear plasma skimming law, equation (5), is solved by the numerical algorithm 1. It first appears that the algorithm does not always converge to a solution but oscillates between two different states with different discharge hematocrit and flow values. Depending on the radius of the mother branch, the range of parameters where the algorithm oscillates, changes (figure 3). The smaller the mother branch radius, the larger the daughter branches radii interval in which no single flow solution is found. When the mother branch radius is above $2.4\mu m$, the oscillating zone separates in two definite regions. These oscillations have different sources.

First when the two daughter branches radii are small, the fractional blood flow FQ^B in one of these branches can go below the threshold $X_o = \dfrac{0.4}{2r_m}$ leading to a discharge hematocrit equal to 0. In this case, the apparent blood viscosity is then equal to that of plasma, which reduces the branch resistance and increases blood flow. At the following iteration, the nonlinear plasma skimming law predicts a positive discharge hematocrit in that branch, increasing strongly the blood apparent viscosity, reducing the simulated blood flow and predicting, at the following iteration, no RBCs. Moreover, the lower the mother branch radius, the higher the threshold X_o, hence the larger the region where these oscillations between iterations occur (figure 3 A).
Second, when daughter branches radii are close, near the $x = y$ line, another region with oscillations appears. The region size depends on the radius of the mother branch as well as on its discharge hematocrit. In this case, $FQ^B < 0.5$ in the smaller branch leads to a decrease of discharge hematocrit in this branch, and then in the next flow computation, to a higher flow in that branch and a lower flow in the other one. As both branches have radii close enough, oscillations appear in the computed flows between iterations. When all radii increase, convergence is always obtained as the effect of plasma skimming lowers.

Yet, the mother branch radius is not the only trigger for the appearance of oscillating zones. When varying the discharge hematocrit in the mother branch, oscillations appear (figure 3 B). The higher the discharge hematocrit, the more important the size of zones where oscillations appear. Similarly to the case of radii variations, two zones exist in which the same behaviors as those described above are observed. Yet, contrary to the observations when varying the radii, the size of the zones where convergence to a single solution is lost varies but these zones never merge within physiological discharge hematocrit values.

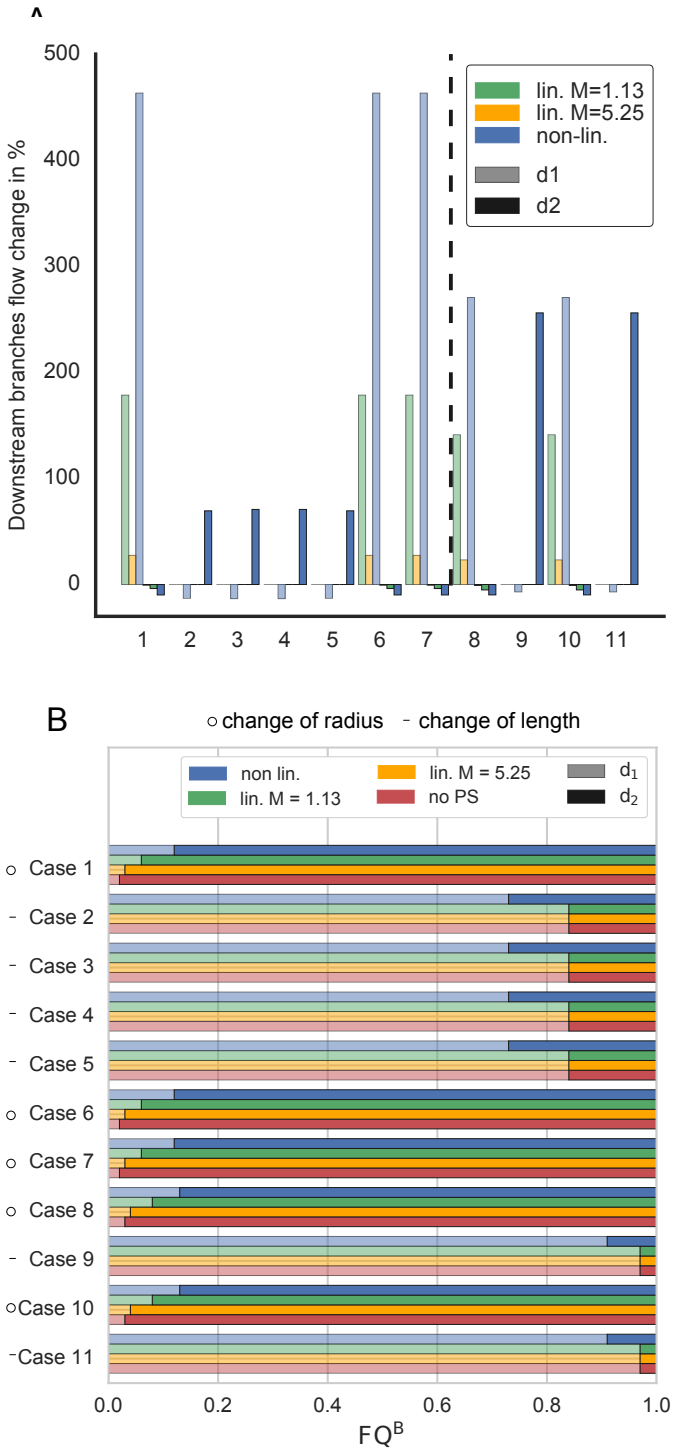

FIGURE 2 Plasma skimming flow study in diverging bifurcations whose geometrical parameters from liver (cases 1 to 7) and kidney (cases 8 to 11) micro-architecture are detailed in table 2. Cases $1, 6-8$ and 10 (o) correspond to variations of branches' radii while the other cases (-) correspond to variations of branches' lengths. (A) For each case, the change of flow induced by three plasma skimming laws (the linear law with two different coefficients M=1.13 and M=5.25 and the nonlinear-law) compared to no plasma skimming is computed in the two daughter branches (3 paler colors for d1, followed by 3 darker colors for d2). (B) For each case, the fractional flows FQ^B are reported for d1 (left) and d2 (right), the sum being 1, for the four studied models, one on each line: without plasma skimming (PS), and with the plasma skimming laws.

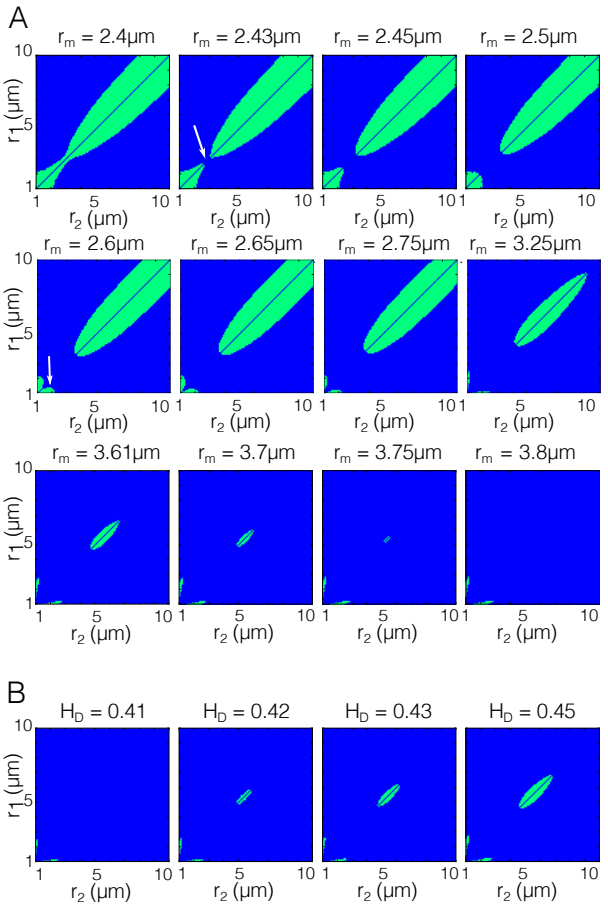

FIGURE 3 Phase diagram for flow solutions in two daughter branches. In the blue regions the algorithm converges to a unique flow solution, while in the green regions the solution oscillates between two states. Number of states depending on the imposed (A) mother branch radius r_m and daughter branch radii r_1 and r_2 for a given $H_D(m) = 0.442$, (B) discharge hematocrit in the mother branch $H_D(m)$ for radius $r_m = 3.61\mu m$ and daughter branch radii r_1 and r_2. Arrows indicate when with increasing r_m, the single non-stationary flow region splits first into two non-stationary flow regions (A first row), then the one with small $r_1 \approx r_2$ splits again into regions (A second row), while at even larger r_m the oscillatory regime at large $r_1 \approx r_2 (\approx 5\mu m)$ disappears (A third raw).

These oscillations hint that blood flow in capillaries may not be steady-state in this situation. These oscillating behaviors of the capillary blood flow have been reported by Krogh[7], and later MacPhee in the liver[9] where capillaries receive successively high discharge hematocrit followed by very few erythrocytes flowing through. Such behaviors could even be reproduced in *in vitro* artificial capillary networks through which blood was pumped[71]. The dynamic system has been studied and it has been shown to have several equilibria[28,72,73,74]. These equilibria stability has been studied, showing different types of behaviors even for simple bifurcations[74]. When the nonlinear plasma skimming law is included, the oscillating states could be related to these observations.

Yet, none of these studies linked these findings to the oscillating states obtained here or varied the discharge hematocrit values. Schmid et. al.[36] also observed oscillations in their dynamic numerical model of erythrocytes in bifurcations, but do not report a parametric study of when such oscillations occur or not.

If the focus is on the removal from blood of compounds that are entering the body through the digestive organs, the duration of such processes is around hours whereas the observed oscillations occur within seconds. In the future, a specific study to simulate both the transport of erythrocytes explicitly along with plasma flow should be pursued, whereby such simulations may serve to determine an averaged solution over time to challenge the results of our studies.

3.1.3 | Study of micro-circulatory representative networks

In the following, the coefficient $M = 1.13$ is discarded as the focus is made on capillary networks and not on bifurcations for which this coefficient was derived (see 2.2). The study of a single bifurcation showed that the asymmetry of radius between downstream branches leads to strong changes in the discharge hematocrit distribution and hence in the simulated blood flow.

Asymmetric trees to mimic micro-vasculature

To determine if this observation can be extended to more complex networks, asymmetric trees (diverging one followed by converging one) are studied, varying between trees the branch radius asymmetry coefficient α (defined in section 22.1).

Including plasma skimming in the model results in having the smallest discharge hematocrit for both laws in the smallest branch (figure 4A): for example for $\alpha = 0.4$, $H_D = 0.0$ with the nonlinear law, and $H_D = 0.34$ for the linear one. This reduction of discharge hematocrit increases blood flow (for $\alpha = 0.4$ by 1100% for the nonlinear law and 27% for the linear law). Yet, for pressure, the maximum difference between the solutions with and without plasma skimming is only 0.067% suggesting that plasma skimming compensates the change in flow Q by a contrary change in viscosity η such that the product $Q \times \eta \propto p$, determing the pressure, remains almost unaltered.

To better quantify changes induced by plasma skimming, the tree's equivalent resistance is studied for several asymmetry coefficients α in figure 4 B. It is computed as:

$$R_{eq} = \frac{P_{inlet} - P_{outlet}}{Q_{inlet}} \tag{34}$$

were P_{inlet} (resp. P_{outlet}) the pressure at the inlet (resp. at the outlet) and Q_{inlet} the blood flow at the inlet. First, it can be noted that for $\alpha = 0.33$, the nonlinear law leads to an oscillation of the numerical algorithm between two states of different resistances. For lower values of α, (or lower values of α^{-1} by symmetry of the tree), the simulations always lead to oscillations (figure 4 B), whereas for $\alpha \in]0.33; 3[$ the algorithm converges to one solution. Between these two states, discharge hematocrit in one of the branches significantly differs (arrows in figure 4 C): one is free from erythrocytes while the other shows a

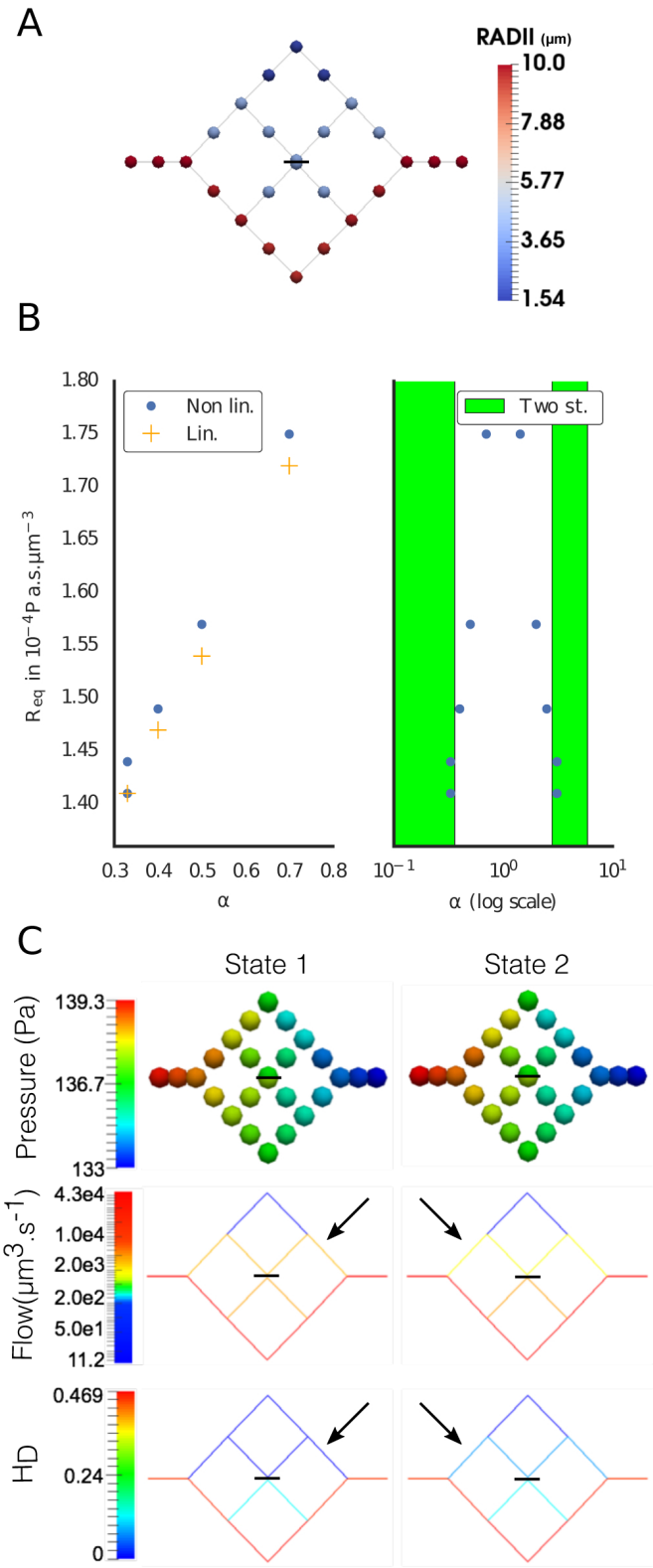

FIGURE 4 (A) Radii at nodes of a converging and diverging asymmetric binary tree for $\alpha = 0.4$. (B) Evolution of the equivalent resistance R_{eq} as a function of the asymmetric tree parameter. Left: for the linear and nonlinear laws. Right: zoom-out for the nonlinear law, exhibiting two-state zones (green, 2 dots per α) for low α and by symmetry for high α. (C) When two states are found, their spatial patterns differ mostly in the flow and hematocrit distribution (see arrows) rather than pressure. Horizontal marks in A and C indicate that the central nodes are disconnected.

strictly positive discharge hematocrit. This behaviour can be related to the parameter study performed in a bifurcation where two states could be found when branch radii are low. The flow going through the erythrocytes' free branch is significantly higher (by 43%) than in the other case. The equivalent resistance is also different (figure 4 B). Additionally to what was found when comparing the solution to no plasma skimming above, there is barely any difference of pressure between the two states: the maximum difference is 0.09%. The lack of a convergent result for idealized networks of similar radii was also found in [20].

Baseline hemodynamics solution in healthy vs. damaged geometry

Next, hemodynamics is simulated in three representative liver lobules (LL), denoted as constant (CLL), healthy (HLL) and dilated (DLL) liver lobule, differing only by their radius (table 3). For CLLs the radius is constant and set to the average of reported literature values, for HLLs, radii are drawn from a Gaussian distribution with the same average as the CLL. For a DLL, which might represent a damage case, the centrilobular sinusoids are dilated. This represents liver damage found due to congestive hepatopathy [75], drug-induced damage [76] and even due to COVID-19 pathology [77].

Blood enters a liver lobule from the PT located in the hexagon's corners, where the highest pressures are observed (figure 5A). It flows towards the CV where the lowest pressures are observed (figure 5A) dispersing over the network such that its distribution represents the pathway with lowest resistance between the PTs and the CV. By contrast to a single *representative* sinusoid that goes from PT to CV, which is a model often used for simplicity to represent a lobule, the velocity along the PT-CV axis is not constant. In addition to velocity being higher on that axis, there is an inhomogeneity in the polar angle between different PT-CV axes. A similar pattern can be seen for pressure and wall shear stress (figure SI 15). When comparing a single sinusoid of the same radius and length as the CLL network to this network, although the imposed pressure difference is almost the same, velocity nearly doubles (77% increase) and the resistance is two orders of magnitude higher (Table 1 last line vs Table 3 2nd line). This highlight the difficulty of defining a 'representative' sinusoid: its definition depends on the quantity of interest (pressure, velocity, flow rate resistance,...).

No plasma skimming: First, blood flow is simulated without plasma skimming (*baseline*). Drawing radii from a Gaussian distribution (HLL) only marginally increases heterogeneity in flow distribution (+4% in standard deviation of the computed flow distribution). But this is enough to increase the equivalent resistance by 35% due to the distribution of diameters (table 3). However, the difference in pressure pattern is not as striking as between the HLL and DLL (figure 5A). As expected, when the zone close to the CV is dilated as in a DLL, the zone with low pressure is wider than in healthy geometries. The flow distribution is more heterogeneous: the standard deviation of the computed flow distribution in the DLL increases by 30%. The median flow over all branches in the DLL, for an identical driving pressure difference, is around 300% that of a HLL, and the total flow going through the network is 40% higher in case of a DLL. Hence, the resistance of the lobule

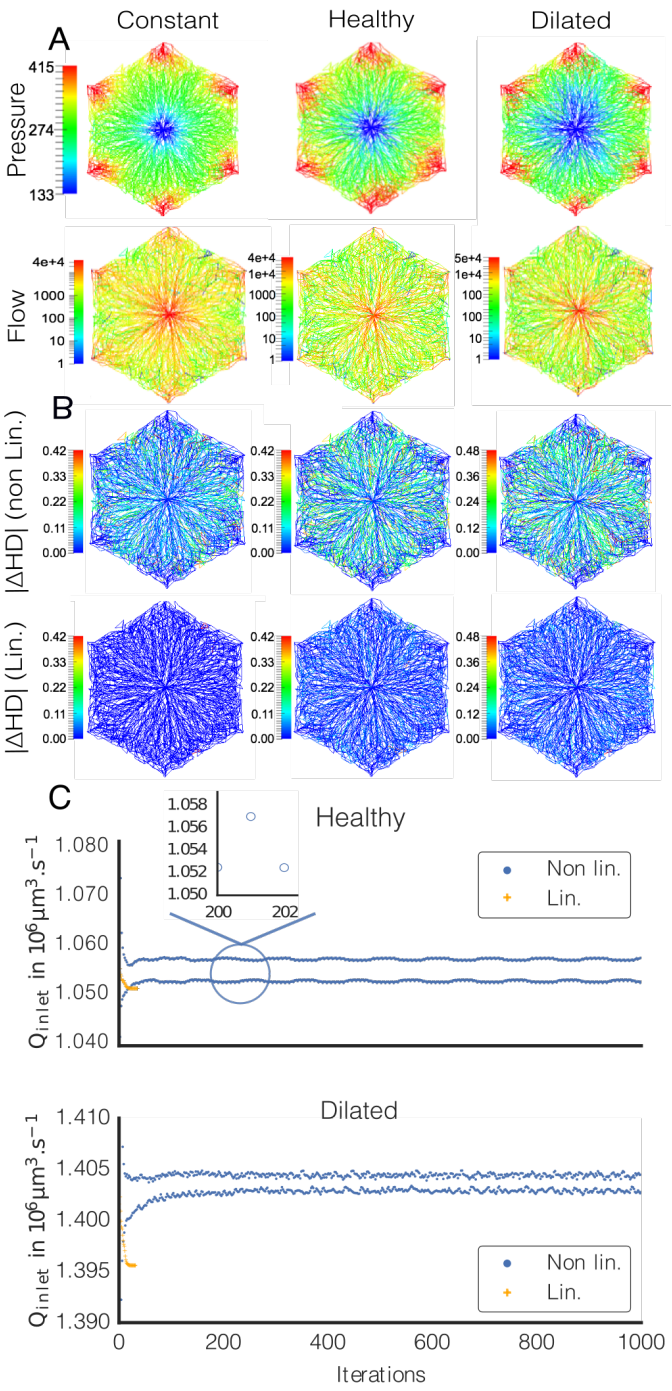

FIGURE 5 (A) Spatial distribution of pressures (in Pa) and flow (in $\mu m^3.s^{-1}$ when no plasma skimming is included in each three studied geometries, classified in the text as CLL, HLL and DLL (= XL(iver)L(obule), X=C(onstant), H(ealthy), D(ilated)). (B) depicts the effect of plasma skimming for both the linear and nonlinear laws on discharge hematocrit as the absolute difference between the predicted discharge hematocrit and the constant value of 0.442. (C) shows the evolution of the total flow crossing the studied liver lobule as a function of iterations for the healthy and dilated lobules for both the linear and nonlinear laws. It underlines that the nonlinear law does not converge to a unique solution but oscillates between two groups of solutions.

is significantly lower in case of a DLL than when a HLL is considered (table 3).

Plasma skimming: Next, plasma skimming laws are considered in each one of the three geometries (figure 5B). The absence of radii variations in the capillary network as a CLL leads to a single state with the algorithm 1 for both laws. If the vessels' radii are drawn from Gaussian distributions (HLL) and the nonlinear law is applied, the algorithm 1 does not converge to a unique flow solution (figure 5C), reminiscent of the observations for varying radii at bifurcations (figure 3). Instead, it oscillates between two groups of states with similar behaviors, but different total flows going through the geometry for the same pressure boundary conditions. In the following, we approximate the nonlinear flow solution by the average over the last one hundred states.

As for simple bifurcations, introducing plasma skimming into the model reduces the number of branches with very low flow, below $50\mu m^3.s^{-1}$ corresponding to a velocity below $2\mu m.s^{-1}$. For the nonlinear law, this number decreases by 18% for the CLL and around 39% for the two other lobules HLL and DLL. For the linear law, the decrease is significantly smaller: below 5% independently of the geometry. This is explained by the reduction of discharge hematocrit in branches with low flow. It induces a drop in the average discharge hematocrit in the network, from 0.442 to 0.41 in the a CLL, and to 0.38 in a DLL both for the nonlinear law. Such decrease of the average discharge hematocrit is consistent with experimental observations in [23] reporting a lower discharge hematocrit in the capillary network than in the rest of the circulatory system. The discharge hematocrit patterns are largely unaffected by plasma skimming for the linear law, while for the nonlinear law, a radii-dependent impact could be observed (figure 5B).

The main differences observed are in the triangular-segmental regions between the main flow pathways, the latter being around the connecting line of PTs and CV (figure 5B). Moreover, for the nonlinear law, if the discharge hematocrit is reduced in average (figure SI 13), the fraction of branches with a discharge hematocrit below 0.05, reported to be around 10% in other networks by Gould and Linninger [21], is here below 2% independently of the studied network.

Finally, the effect of plasma skimming on the pressure distribution is very limited (figures SI 10, 11, 12), which was observed in the asymmetric tree; and so is the effect on the wall-shear stress, which can be explained by the choice of pressure boundary conditions and the compensation effect between η and Q (as $\tau \sim \eta Q$) (figure SI 15). This is consistent with a study on cerebral microcirculation [34].

The linear model effect can be neglected compared to the nonlinear law

In each geometry, the median difference to the baseline solution is computed for both simulated discharge hematocrit and flow. As for bifurcations, the linear law leads to differences significantly lower than those induced by the nonlinear law: around three to four fold lower for the HLL and DLL, and more than a hundred fold for the CLL (figure SI 14).

Changes induced by the pathology or damage are more important than those induced by plasma skimming

Finally, regardless of the plasma skimming law, the difference induced by a change of sinusoid radius (table 3) is significantly higher than those induced by plasma skimming. This can be seen by the pressure and flow pattern differences in 5A more striking than within each figure SI 10,11,12), and similarly for WSS in figure SI 15. To have differences within the same order of magnitude, the change of radius would need to introduce a median flow difference below 20% (figure SI 14) which represents, roughly, a change of radius below 5%. Such radius change would however not be considered pathological as it can be observed between different regions in a lobule.

3.2 | Compound convection-reaction in micro-vasculature

With the flow field computed as described in the previous sections, it is then possible to transport a concentration time-varying profile in the network. In this section, the considered flow profile does not include plasma skimming as this is not needed to be able to discriminate between HLLs and DLLs.

3.2.1 | Study of the proposed convection finite volume scheme

Properties for the pure convection case

- *Property 1* The numerical scheme using fluxes of (26) is positivity conserving under specific CFL conditions. The proof of this property can be found in the appendix.
- *Property 2* The numerical scheme using fluxes of (26) is mass conserving by construction.

Even though the CFL condition is set to (20), in practice the numerical scheme with fluxes as in (26) is positivity preserving.

The relative L_2 error at the outlet of a symmetric converging bifurcation or diverging bifurcation, with constant radius $r = 3.61\mu m$ and length representing on lobule branch's length, and considering a Gaussian time input concentration, is defined as:

$$L_2 = \frac{\sqrt{\sum_{n\in T}(\frac{U^n_{out}}{V_{out}} - \frac{U^{n,*}_{out}}{V_{out}})^2}}{\sqrt{\sum_{n\in T}(\frac{U^{n,*}_{out}}{V_{out}})^2}} \tag{35}$$

with $U^{n,*}_{out}$ the solution with the smallest space step set to $0.25\mu m$ corresponding to one tenth of the first studied space step. It appears that the proposed numerical scheme with flux limiters leads to lower errors than the upwind scheme that is of first order (figure 6). Yet, the convergence rate is not second order. This can be explained by the choice of boundary condition at the outlet that are first order and the effect of the bifurcation on the error. Moreover, it can be noted that the flux limiters (Superbee, MC, MinMod, VanLeer) give an error slightly higher than that

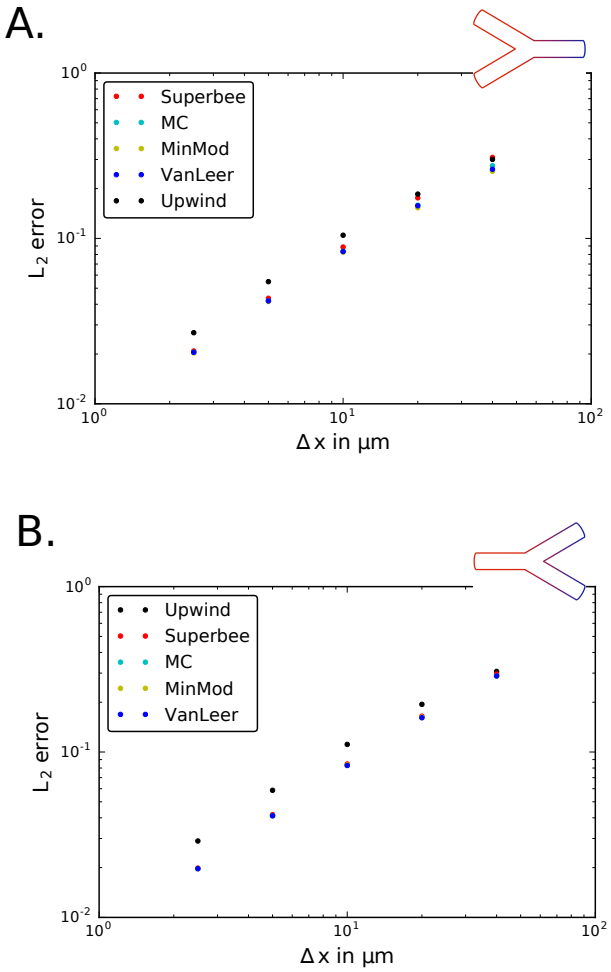

FIGURE 6 Relative L_2 error of the solution obtained at the outlet of a symmetric converging bifurcation (A) and diverging bifurcation (B) with radius $r = 3.61\mu m$, imposed velocity at the inlet for A (resp. outlet for B) of $80\mu m.s^{-1}$ to reproduce velocities obtained in liver lobules with space steps of $[2.5, 5.0, 10.0, 20.0, 40.0]\mu m$ corresponding to CFL (20) $\in [0.5, 0.25, 0.125, 0.0625, 0.03125]$ to the solution with a space step set to $0.25\mu m$ corresponding to CFL (20) equals to 1. The upwind solution is above the others; when non-distinguishable, all the non-upwind solutions are superimposed.

of the upwind scheme in a converging bifurcation for very small space steps. This is explained by the appearance of a slight overshoot of the limiters due to the fact that under the chosen CFL condition of equation (20), the scheme may not satisfy the maximum principle.

Moreover, both the Superbee and VanLeer schemes seem to lead to higher errors than the MC and MinMod limiters. Depending on the precision needed by the application, the flux limiter scheme with either the MC or MinMod limiters permits to reduce the resulting numerical scheme error.

3.2.2 | Study of different convection-reaction regimes

After proposing a numerical scheme to simulate a convection equation in a network that reduces the numerical diffusion, this scheme is extended to a convection-reaction equation as described in section 2.3.1. To underline the importance of having a precise numerical scheme, convection-reaction is studied in a single blood vessel along which cells are aligned. The asymptotic behaviors (depicted in equations (14) and (13)) of a Michaelis-Menten reaction term are first studied to better understand the effect of reaction on the bolus shape. A Gaussian concentration input is set at the tube inlet, and the computed concentration profile at the outlet is compared with the analytic solution coming from the characteristics methods when it can be computed, as detailed in SI 6.3. Convection velocity is set to the average measured value (i.e. $138.8\mu m.s^{-1}$) and the time step is set such that it respects the CFL.

Linear reaction limit

The reaction term tends to be proportional to the concentration in blood. If the reaction rate is very low compared to the convection velocity, the bolus is convected through the tube and is not taken up by the surrounding cells (figure 7A). When higher, the linear reaction term induces an exponential loss of the injected concentration amplitude (see equation (54)): the compound is mainly taken up by the cells, and will be removed entirely after a single passage through the capillaries. Yet, it does not seem to impact on the bolus duration (i.e. time during which the input function shape is above zero) (figure 7B). If the upwind scheme seems close to the analytic solution when the reaction speed is high enough, it is not the case when reaction goes down to zero, showing the need for a higher order numerical scheme.

Saturated reaction limit

In case of a saturated reaction limit, the nonlinear term converges to a constant, which means a constant amount of compound is removed from the blood. With a saturated exchange, the concentration curve amplitude decreases linearly with time (figure 7C) as expected by the analytical solution (see equation (54)). Here, the choice of numerical scheme is even more important than for the linear exchange case as the upwind scheme strongly overestimates the amplitude loss and the bolus duration throughout the tube.

Michaelis-Menten kinetics

Finally, an active-saturated exchange (following the Michaelis-Menten kinetics, equation (12)) is considered. Both above mentioned phenomena are observed here. First, the bolus length (i.e. space between the start of the curve and its end) is conserved as it is the case for a linear reaction term. Then, similarly to the saturated case, its amplitude decreases linearly with time (figure 7D). As expected from the two previous cases again a higher order scheme is needed to accurately account for the effect of the reaction term on the bolus shape.

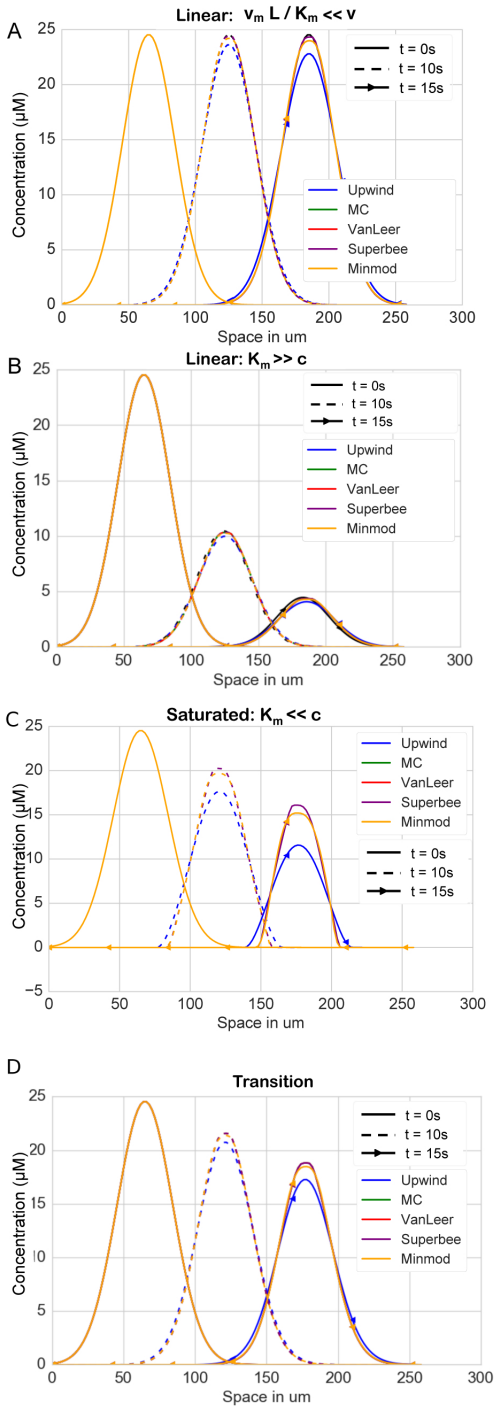

FIGURE 7 Compound concentration at the outlet of a tube along which a row of cells is aligned for different times and numerical schemes. (A) depicts the case of a linear reaction term with convection overwhelming reaction ($v_{r,max}$ very small), (B) when reaction overwhelms convection ($v_{r,max}/K_{r,max} = 10s^{-1}$), (C) the case of a saturated reaction term ($v_{r,max} = 10\mu M/s$ and $K_{r,max} = 0.01\mu M$) and (D) a case of a Michaelis-Menten reaction term ($v_{r,max} = 10\mu M/s$ and $K_{r,max} = 10\mu M$). Most solutions are superimposed with the analytical solution (black line) when it exists, i.e. for the linear and saturated regimes (see SI 6.3).

TABLE 5 Mean Transit Times computed with equation (29) in four different networks: one with a constant radius, one with a constant radius and a dilated peri-central area, a healthy network with radii drawn from a Gaussian and finally a healthy network with a dilated peri-central area in which radii are drawn from a Gaussian.

	CLL	Const. Dilated LL	HLL	DLL
$\bar{T}$ in s	29.7	28.9	31.4	30.3

3.2.3 | Dispersion effect of healthy vs. damaged entire liver lobule

Pure convection behavior in networks for different bolus shapes

Now looking at a whole network, different types of boli are tested with MC slope limiter as it seems the most versatile one to capture most of the potential concentration inputs that can occur in liver microarchitecture. Incorporating flux limiters lowers numerical diffusion for two bolus cases (figure 8). First, two sharp boli, a rectangular function and a short Gaussian close to a Dirac, are studied. The influence of the network appears slightly in the rectangle input function, but is stronger for the short Gaussian function where the constant network disperses less the bolus than the two other networks. Then, two smooth boli are considered, a wide Gaussian, and Parker's Arterial Input Function[78]. In both cases, the effect of the network on the bolus shape is significantly lower than that for sharp inputs.

Imposing a Gaussian input in the three liver lobule capillary networks, the mean transit time is computed with equation (29). Increasing the peri-central radii leads to an increase of the blood velocity there, hence diminishes the mean transit time compared to a healthy case (table 5). Additionally, drawing radii from a Gaussian instead having a constant radius slightly increases the mean transit time which can be explained as the average velocity in these networks are slightly lower than for a constant radius. This difference is similar to that introduced by a dilatation of the peri-central area showing that such indicators alone do not permit to diagnose such anatomical alterations.

4 | CONCLUSION

A mathematical model of blood detoxification by a liver lobule has been successively built up from building blocks that captures key components of that process and hence may serve as a reference model for future applications or extensions. The considered building blocks were flow, the impact of RBC, geometrical elements such as tubes, bifurcations, and simplified and entire capillary networks, different temporal concentration kinetics of transported compounds, and different types of compound uptake kinetics from the blood into the cell. The model built-up was accompanied by a study of numerical algorithms and schemes to facilitate their right choice. The final model encompasses a hemodynamics model coupled with a convection-reaction equation in detoxifying

organs in general and in a liver lobule in particular. Several geometries, from a simple tube to a whole capillary network, that was sampled from full volume data sets of real liver lobules in mouse[44], were considered to better understand the importance of including the effects of RBCs on hemodynamics. Regarding the blood flow model, features that need to be included to reproduce the average blood flow velocities observed biologically were discussed. For capillaries as those in liver lobules, the Fahraeus-Lindqvist effect was needed to be taken into account as otherwise model and data disagree. Moreover, plasma skimming homogenised flow at bifurcations while having minor influence on pressure and wall shear stress. The linear skimming law proposed by Gould & Linninger[21] was found to impact significantly less on hemodynamics and hematocrit distribution than the nonlinear law from Pries et.al.[19]. Our interpretation of numerical results for the latter law is that the system can switch between different states, coherently with the experimental and modelling literature. Two parameter regions for which multiple states appear were found. In small capillaries of diameter $\sim 2-6\mu m$ but rather uneven between the two daughter (outflow-carrying) branches, oscillations of hematocrit levels between zero and a positive value were found. By contrast, in larger capillaries when the two daughter branches were of similar radii, oscillations were obtained with none of the branches being free of erythrocytes. The magnitude of the daughter radii (r_1, r_2) at which oscillations were observed depended on the radius of the mother (inflow-carrying) branch and its hematocrit.

A future improved model could include the transport of hematocrit in blood coupled with Poiseuille flow for the blood plasma. Yet, such a non-stationary model of blood flow would have a high computational cost and might not be suited when applied to detoxification prediction of compounds over several hours and in entire capillary networks. This issue might be solved by time-averaging over found oscillatory solutions and then working with the average in a stationary blood flow model. It would be interesting to see if the so found solutions relate to the states obtained in this study.

Regarding the use of a single sinusoid as a reduced model of a whole lobule, our results show that such single sinusoid may not be representative of the heterogeneous hemodynamics seen along the portal triad - central vein axis but also angularly between these axes. If a single sinusoid model is sought, more work is warranted to derive a better representative reduced model and assess its deviation from a 3D network for transport.

Concerning rheology, by contrast to the Fahraeus-Lindqvist effect, plasma skimming can be neglected when studying the consumption of compounds transported with the blood into liver lobule networks. In our studies, which were guided by microarchitectural arrangements of capillaries in hepatic lobules, and for which the geometric parameter ranges were chosen accordingly, the difference in pressure and flow patterns induced by variation of capillary diameter, such as dilatation of the sinusoids observed in disease situations, is significantly higher than the difference between including plasma skimming (even for the nonlinear law) or not. The flow homogenization effect of plasma skimming seen in bifurcations is negligible in these networks.

Here we used *statistically representative* liver lobules because entire liver lobules together with their portal feeding vessels and central vein could not directly be reconstructed in 3D[44,1]. In light of the hemodynamics sensitivity to sinusoidal diameter distributions in our simulations, careful experiments to reconstruct entire lobules would be recommended, which should be feasible with the most recent generation of high-resolution microscopies (such as newest confocal laser scanning, or multi-photon microscopes). Targeted experiments could further assess the validity of these models and conclude on a consistent hierarchy of validated consensus models sorted by their spatial and temporal resolution. They should be combined with simulations in real entire liver lobules sampled at different locations of the liver and, ideally, with intravital imaging to capture the relation between velocity field and architecture. Such future work should include to derive more specific laws, from refined simulations that include RBC deformability[79] in bifurcations[80], accompanied by proper experimental setups[81,82], ideally complemented with intravital hemodynamics studies.

To study spatial compound transport in combination with its removal from the blood, convection-reaction equations need to be accurately solved in network-like structures. For this, a numerical scheme for the transport equation handling multi-furcations and reduction of numerical diffusion is proposed: it is positivity preserving and mass conserving. It performs better than the upwind scheme for a number of common flux limiters, on simple and complex networks, for different types of input function temporal shapes. Moreover, this study underlines the need to have an accurate scheme when considering different types of reaction, especially when simulating first pass effects. Comparison of upwind scheme and various flux limiters shows that MC, VL and Superbee limiters perform best in these 1D pipes, for which the solution could be analytically verified. The proposed numerical scheme could be adapted to simulate the transport of erythrocytes (RBCs) in order to dynamically study hemodynamics in micro-architecture.

A further extension would be to couple the hemodynamics including RBCs with the convection-reaction of a compound to study the first pass effect of the injection of a bolus in an organ micro-architecture. Because for some metabolites, the long-time solution is of interest, the steady state flow pattern obtained by averaging the blood flow solution over time could be sufficient to consider before simulating the convection-reaction problem.

Finally, simulations in a liver lobule suggest that the mean transit time might not be an injury signature in case of pericentral widening despite the latter affects the hemodynamics.

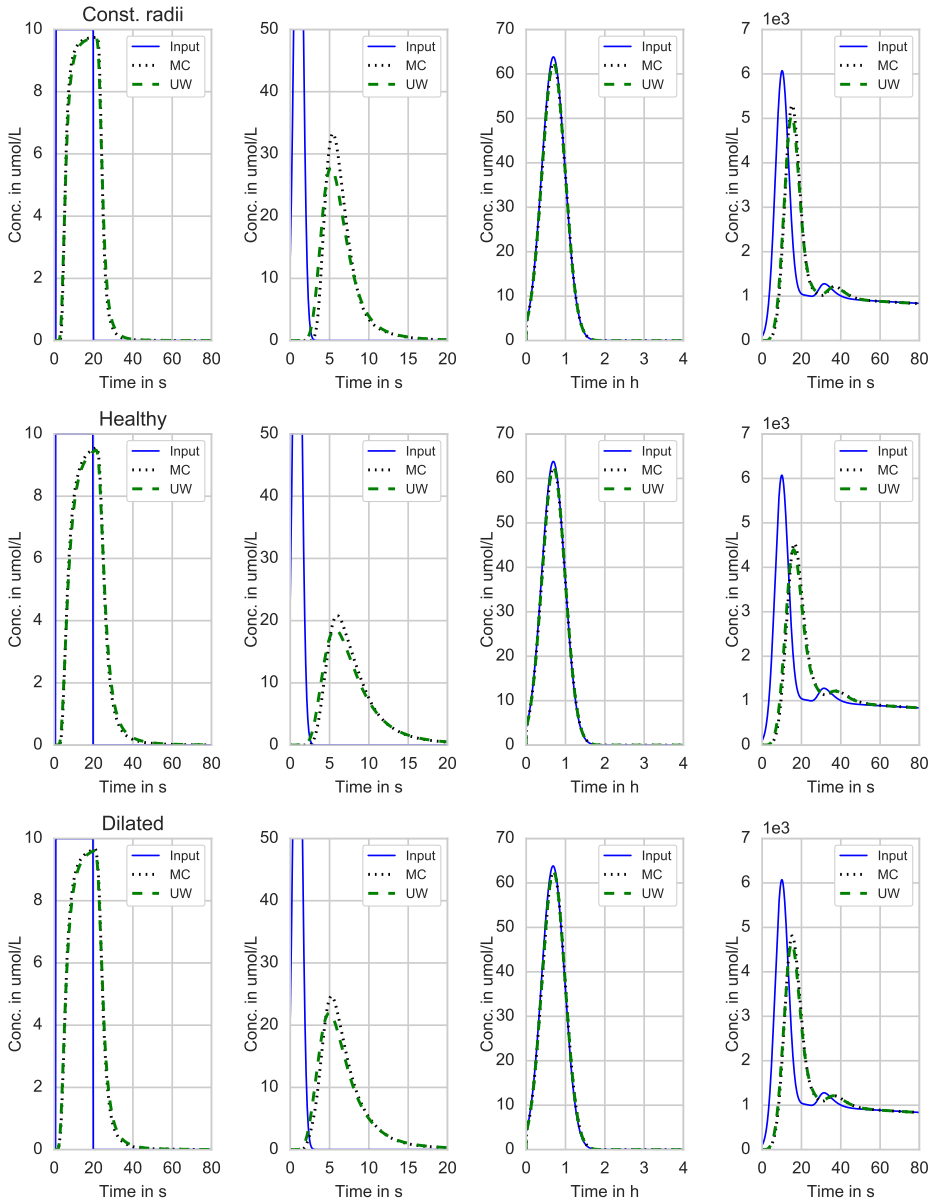

FIGURE 8 Convection of different boli shapes in the three previously studied liver lobule networks (top row: CLL, middle row: HLL, last row: DLL) to cover most shapes that could be observed for concentration inputs in liver. Two sharp boli, a rectangular function (1st column) and a short Gaussian close to a Dirac (2nd column), are followed by two smooth boli, a wide Gaussian (3rd column), and a typical dynamic imaging input curve - Parker's Arterial Input Function[78] (4th column). The input curve injected in the PV is in blue, while the concentration in the CV network outlet is plotted for the upwind (UW) and MC numerical schemes.

DATA ACCESSIBILITY

The code for the proposed numerical scheme is available at https://gitlab.inria.fr/reo/transport-in-1d-networks.

ACKNOWLEDGMENTS

This work has been supported by the German Ministry of Education and Research through LiSym (Grant No. 031L0045, BMBF) and the French Ministry of Research through the grants iFlow (ANR-13-TECS-0006) and iLite (ANR-16-RHUS-0005). The authors would like to thank Damiano Lombardi (INRIA) for numerical insights in this work.

References

1. Hammad S, Hoehme S, Friebel A, et al. Protocols for staining of bile canalicular and sinusoidal networks of human, mouse and pig livers, three-dimensional reconstruction and quantification of tissue microarchitecture by image processing and analysis. *Archives of toxicology* 2014; 88(5): 1161–1183.

2. Ghallab A, Hofmann U, Sezgin S, et al. Bile microinfarcts in cholestasis are initiated by rupture of the apical hepatocyte membrane and cause shunting of bile to sinusoidal blood. *Hepatology* 2019; 69(2): 666–683.

3. Lipowsky H, Zweifach B. Network analysis of microcirculation of cat mesentery. *Microvascular research* 1974; 7(1): 73–83.

4. Zweifach BW, Lipowsky HH. Quantitative studies of microcirculatory structure and function. III. Microvascular hemodynamics of cat mesentery and rabbit omentum.. *Circulation Research* 1977; 41(3): 380–390.

5. Fronek K, Zweifach BW. Microvascular pressure distribution in skeletal muscle and the effect of vasodilation. *American Journal of Physiology–Legacy Content* 1975; 228(3): 791–796.

6. Pries A, Ley K, Gaehtgens P. Generalization of the Fahraeus principle for microvessel networks. *American Journal of Physiology-Heart and Circulatory Physiology* 1986; 251(6): H1324–H1332.

7. Krogh A. Studies on the physiology of capillaries: II. The reactions to local stimuli of the blood-vessels in the skin and web of the frog. *The Journal of physiology* 1921; 55(5-6): 412.

8. Klitzman B, Johnson PC. Capillary network geometry and red cell distribution in hamster cremaster muscle. *American Journal of Physiology-Heart and Circulatory Physiology* 1982; 242(2): H211–H219.

9. MacPhee P, Schmidt E, Groom A. Intermittence of blood flow in liver sinusoids, studied by high-resolution in vivo microscopy. *American Journal of Physiology-Gastrointestinal and Liver Physiology* 1995; 269(5): G692–G698.

10. Clavica F, Homsy A, Jeandupeux L, Obrist D. Red blood cell phase separation in symmetric and asymmetric microchannel networks: effect of capillary dilation and inflow velocity. *Scientific reports* 2016; 6: 36763.

11. Sun C, Munn LL. Particulate nature of blood determines macroscopic rheology: a 2-D lattice Boltzmann analysis. *Biophysical journal* 2005; 88(3): 1635–1645.

12. Fedosov DA, Caswell B, Karniadakis GE. A multiscale red blood cell model with accurate mechanics, rheology, and dynamics. *Biophysical journal* 2010; 98(10): 2215–2225.

13. Pan W, Fedosov DA, Caswell B, Karniadakis GE. Predicting dynamics and rheology of blood flow: a comparative study of multiscale and low-dimensional models of red blood cells. *Microvascular research* 2011; 82(2): 163–170.

14. Pries A, Secomb T, Gessner T, Sperandio M, Gross J, Gaehtgens P. Resistance to blood flow in microvessels in vivo.. *Circulation research* 1994; 75(5): 904–915.

15. Sharan M, Popel AS. A two-phase model for flow of blood in narrow tubes with increased effective viscosity near the wall. *Biorheology* 2001; 38(5, 6): 415–428.

16. Dellimore JW, Dunlop MJ, Canham PB. Ratio of cells and plasma in blood flowing past branches in small plastic channels. *American Journal of Physiology-Heart and Circulatory Physiology* 1983; 244(5): H635–H643.

17. Carr RT, Wickham LL. Plasma skimming in serial microvascular bifurcations. *Microvascular research* 1990; 40(2): 179–190.

18. Fenton BM, Carr RT, Cokelet GR. Nonuniform red cell distribution in 20 to 100 μm bifurcations. *Microvascular research* 1985; 29(1): 103–126.

19. Pries A, Ley K, Claassen M, Gaehtgens P. Red cell distribution at microvascular bifurcations. *Microvascular research* 1989; 38(1): 81–101.

20. Guibert R, Fonta C, Plouraboué F. A new approach to model confined suspensions flows in complex networks: application to blood flow. *Transport in porous media* 2010; 83(1): 171–194.

21. Gould IG, Linninger AA. Hematocrit distribution and tissue oxygenation in large microcirculatory networks. *Microcirculation* 2015; 22(1): 1–18.

22. Popel AS, Johnson PC. Microcirculation and hemorheology. *Annu. Rev. Fluid Mech.* 2005; 37: 43–69.

23. Pries AR, Secomb TW. *Blood Flow in Microvascular Networks*ch. 1: 3-36; American Cancer Society . 2011

24. Debbaut C, De Wilde D, Casteleyn C, et al. Modeling the impact of partial hepatectomy on the hepatic hemodynamics using a rat model. *IEEE Transactions on Biomedical Engineering* 2012; 59(12): 3293–3303.

25. Peyrounette M, Davit Y, Quintard M, Lorthois S. Multiscale modelling of blood flow in cerebral microcirculation: Details at capillary scale control accuracy at the level of the cortex. *PloS one* 2018; 13(1): e0189474.

26. Possenti L, Gregorio dS, Gerosa FM, et al. A computational model for microcirculation including Fahraeus-Lindqvist effect, plasma skimming and fluid exchange with the tissue interstitium. *International Journal for Numerical Methods in Biomedical Engineering* 2019; 35(3): e3165.

27. Geddes JB, Carr RT, Wu F, Lao Y, Maher M. Blood flow in microvascular networks: A study in nonlinear biology. *Chaos: An Interdisciplinary Journal of Nonlinear Science* 2010; 20(4): 045123.

28. Carr RT, Geddes JB, Wu F. Oscillations in a simple microvascular network. *Annals of biomedical engineering* 2005; 33(6): 764–771.

29. Pozrikidis C. Numerical simulation of blood flow through microvascular capillary networks. *Bulletin of mathematical biology* 2009; 71(6): 1520–1541.

30. Watson M, McDougall S, Chaplain M, Devlin A, Mitchell C. Dynamics of angiogenesis during murine retinal development: a coupled in vivo and in silico study. *Journal of The Royal Society Interface* 2012: rsif20120067.

31. Chaplain MA, McDougall SR, Anderson A. Mathematical modeling of tumor-induced angiogenesis. *Annu. Rev. Biomed. Eng.* 2006; 8: 233–257.

32. Pillay S, Byrne H, Maini P. Multiscale Modeling of Angiogenesis and Predictive Capacity. *Bulletin of the American Physical Society* 2017; 62.

33. Drasdo D, Jagiella N, Ramis-Conde I, Vignon-Clementel I, Weens W. Modeling steps from a benign tumor to an invasive cancer: examples of intrinsically multi-scale problems. *Cell Mechanics: From Single Scale-Based Models to Multiscale Modeling, Chapman & Hall/CRC* 2010: 379–417.

34. Guibert R, Fonta C, Plouraboué F. Cerebral blood flow modeling in primate cortex. *Journal of Cerebral Blood Flow & Metabolism* 2010; 30(11): 1860–1873.

35. Gould IG, Tsai P, Kleinfeld D, Linninger A. The capillary bed offers the largest hemodynamic resistance to the cortical blood supply. *Journal of Cerebral Blood Flow & Metabolism* 2017; 37(1): 52–68.

36. Schmid F, Reichold J, Weber B, Jenny P. The impact of capillary dilation on the distribution of red blood cells in artificial networks. *American Journal of Physiology-Heart and Circulatory Physiology* 2015; 308(7): H733–H742. doi: 10.1152/ajpheart.00335.2014

37. LeVeque RJ. *Finite volume methods for hyperbolic problems*. 31. Cambridge university press . 2002.

38. Canic S, Piccoli B, Qiu JM, Ren T. Runge–Kutta Discontinuous Galerkin Method for Traffic Flow Model on Networks. *Journal of Scientific Computing* 2015; 63(1): 233–255.

39. Russell TF, Celia MA. An overview of research on Eulerian–Lagrangian localized adjoint methods (ELLAM). *Advances in Water resources* 2002; 25(8): 1215–1231.

40. Schwen LO, Krauss M, Niederalt C, et al. Spatio-temporal simulation of first pass drug perfusion in the liver. *PLoS Comput Biol* 2014; 10(3): e1003499.

41. Schwen LO, Schenk A, Kreutz C, et al. Representative Sinusoids for Hepatic Four-Scale Pharmacokinetics Simulations. *PloS one* 2015; 10(7): e0133653.

42. Franiatte S, Clarke R, Ho H. A computational model for hepatotoxicity by coupling drug transport and acetaminophen metabolism equations. *International Journal for Numerical Methods in Biomedical Engineering* 2019. doi: doi: 10.1002/cnm.3234

43. Zamir M. On fractal properties of arterial trees. *Journal of theoretical biology* 1999; 197(4): 517–526.

44. Hoehme S, Brulport M, Bauer A, et al. Prediction and validation of cell alignment along microvessels as order principle to restore tissue architecture in liver regeneration. *Proceedings of the National Academy of Sciences* 2010; 107(23): 10371–10376.

45. Theruvath T, Zhong Z, Currin R, Ramshesh V, Lemasters J. Endothelial Nitric Oxide Synthase Protects Transplanted Mouse Livers Against Storage/Reperfusion Injury: Role of Vasodilatory and Innate Immunity Pathways. *Transplantation Proceedings* 2006; 38(10): 3351 - 3357. doi: http://dx.doi.org/10.1016/j.transproceed.2006.10.171

46. Sidler D, Studer P, Küpper S, et al. Granulocyte colony-stimulating factor increases hepatic sinusoidal perfusion during liver regeneration in mice. *Journal of investigative surgery* 2008; 21(2): 57–64.

47. Yoon YJ, Chang S, Kim OY, et al. Three-dimensional imaging of hepatic sinusoids in mice using synchrotron radiation micro-computed tomography. *PloS one* 2013; 8(7): e68600.

48. Vollmar B, Siegmund S, Menger MD. An intravital fluorescence microscopic study of hepatic microvascular and cellular derangements in developing cirrhosis in rats. *Hepatology* 1998; 27(6): 1544–1553.

49. Dill MT, Rothweiler S, Djonov V, et al. Disruption of Notch1 induces vascular remodeling, intussusceptive angiogenesis, and angiosarcomas in livers of mice. *Gastroenterology* 2012; 142(4): 967–977.

50. Chen J, King K, Zhang JX. Effect of caloric restriction on hepatic sinusoidal system and stellate cells in mice. *Journal of aging research* 2014; 2014.

51. Vanheule E, Geerts AM, Reynaert H, et al. Influence of somatostatin and octreotide on liver microcirculation in an experimental mouse model of cirrhosis studied by intravital fluorescence microscopy. *Liver International* 2008; 28(1): 107–116.

52. Eguchi H, McCuskey PA, McCuskey RS. Kupffer cell activity and hepatic microvascular events after acute ethanol ingestion in mice. *Hepatology* 1991; 13(4): 751–757.

53. Aidoo E, Addai FK, Ahenkorah J, Hottor B, Bugyei KA, Gyan BA. Natural cocoa ingestion reduced liver damage in mice infected with Plasmodium berghei (NK65). *Research and Reports in Tropical Medicine* 2012.

54. Adamczak M, Gross ML, Amann K, Ritz E. Reversal of glomerular lesions involves coordinated restructuring of glomerular microvasculature. *Journal of the American Society of Nephrology* 2004; 15(12): 3063–3072.

55. Remuzzi A, Brenner BM, Pata V, et al. Three-dimensional reconstructed glomerular capillary network: blood flow distribution and local filtration. *American Journal of Physiology-Renal Physiology* 1992; 263(3): F562–F572.

56. Komatsu H, Koo A, Guth PH. Leukocyte flow dynamics in the rat liver microcirculation. *Microvascular research* 1990; 40(1): 1–13.

57. Rocca NA, Walker MG, McCaig LA, et al. The biological effects of lung-derived mediators on the liver. *Experimental lung research* 2011; 37(7): 419–426.

58. Maass-Moreno R, Rothe CF. Distribution of pressure gradients along hepatic vasculature. *American Journal of Physiology-Heart and Circulatory Physiology* 1997; 272(6): H2826–H2832.

59. Shibayama Y, Nakata K. Localization of increased hepatic vascular resistance in liver cirrhosis. *Hepatology* 1985; 5(4): 643–648.

60. Nakata K, Leong G, Brauer R. Direct measurement of blood pressures in minute vessels of the liver. *American Journal of Physiology–Legacy Content* 1960; 199(6): 1181–1188.

61. Kuntz E, Kuntz HD. *Hepatology: Textbook and atlas*. Springer Science & Business Media . 2009.

62. Vorst V. dHA. Bi-CGSTAB: A fast and smoothly converging variant of Bi-CG for the solution of nonsymmetric linear systems. *SIAM Journal on scientific and Statistical Computing* 1992; 13(2): 631–644.

63. Oh S, McDonnell M, Holzbach R, Jamieson A. Diffusion coefficients of single bile salt and bile salt-mixed lipid micelles in aqueous solution measured by quasielastic laser light scattering. *Biochimica et Biophysica Acta (BBA)-Lipids and Lipid Metabolism* 1977; 488(1): 25–35.

64. Michaelis L, Menten ML. Die kinetik der invertinwirkung. *Biochem. z* 1913; 49(333-369): 352.

65. Shu CW. *Essentially non-oscillatory and weighted essentially non-oscillatory schemes for hyperbolic conservation laws*. Springer . 1998.

66. Roe P. Characteristic-based schemes for the Euler equations. *Annual review of fluid mechanics* 1986; 18(1): 337–365.

67. Van Leer B. Towards the ultimate conservative difference scheme III. Upstream-centered finite-difference schemes for ideal compressible flow. *Journal of Computational Physics* 1977; 23(3): 263–275.

68. Van Leer B. Towards the ultimate conservative difference scheme. II. Monotonicity and conservation combined in a second-order scheme. *Journal of computational physics* 1974; 14(4): 361–370.

69. Bassingthwaighte J. Modeling in the analysis of solute and water exchange in the microvasculature. *Handbook of physiology. The cardiovascular system microcirculation* 1984; 4: 549–626.

70. Glenn E. Viscosity. *Physics Hypertextbook* 2010.

71. Shevkoplyas SS, Gifford SC, Yoshida T, Bitensky MW. Prototype of an in vitro model of the microcirculation. *Microvascular research* 2003; 65(2): 132–136.

72. Carr RT, Lacoin M. Nonlinear dynamics of microvascular blood flow. *Annals of biomedical engineering* 2000; 28(6): 641–652.

73. Davis J, Pozrikidis C. Self-sustained oscillations in blood flow through a honeycomb capillary network. *Bulletin of mathematical biology* 2014; 76(9): 2217–2237.

74. Karst NJ, Storey BD, Geddes JB. Oscillations and Multiple Equilibria in Microvascular Blood Flow. *Bulletin of mathematical biology* 2015; 77(7): 1377–1400.

75. DeLeve LD. Vascular liver diseases. *Current gastroenterology reports* 2003; 5(1): 63–70.

76. Furlan A, Minervini MI, Borhani AA, Burgio MD, Tublin ME, Brancatelli G. Hepatic sinusoidal dilatation: a review of causes with imaging-pathologic correlation. In: . 37(6). Elsevier; 2016: 525–532.

77. Tian S, Xiong Y, Liu H, et al. Pathological study of the 2019 novel coronavirus disease (COVID-19) through postmortem core biopsies. *Modern Pathology* 2020: 1–8.

78. Parker GJ, Roberts C, Macdonald A, et al. Experimentally-derived functional form for a population-averaged high-temporal-resolution arterial input function for dynamic contrast-enhanced MRI. *Magnetic resonance in medicine* 2006; 56(5): 993–1000.

79. Lanotte L, Mauer J, Mendez S, et al. Red cells' dynamic morphologies govern blood shear thinning under microcirculatory flow conditions. *Proceedings of the National Academy of Sciences* 2016; 113(47): 13289–13294.

80. Xu D, Kaliviotis E, Munjiza A, Avital E, Ji C, Williams J. Large scale simulation of red blood cell aggregation in shear flows. *Journal of biomechanics* 2013; 46(11): 1810–1817.

81. Kaliviotis E, Sherwood JM, Balabani S. Partitioning of red blood cell aggregates in bifurcating microscale flows. *Scientific Reports* 2017; 7. doi: 10.1038/srep44563

82. Shen Z, Coupier G, Kaoui B, et al. Inversion of hematocrit partition at microfluidic bifurcations. *Microvascular Research* 2016. doi: 10.1016/j.mvr.2015.12.009

83. Bayer IM, Adamson SL, Langille BL. Atrophic remodeling of the artery-cuffed artery. *Arteriosclerosis, thrombosis, and vascular biology* 1999; 19(6): 1499–1505.

84. Lindsey SE, Butcher JT, Vignon-Clementel IE. Cohort-based multiscale analysis of hemodynamic-driven growth and remodeling of the embryonic pharyngeal arch arteries. *Development* 2018; 145(20).

85. Wang Z, Sui Y, Salsac AV, Barthès-Biesel D, Wang W. Motion of a spherical capsule in branched tube flow with finite inertia. *Journal of Fluid Mechanics* 2016; 806: 603–626.

86. Barakat AI. Blood flow and arterial endothelial dysfunction: mechanisms and implications. *Comptes Rendus Physique* 2013; 14(6): 479–496.

87. Fisher AB, Chien S, Barakat AI, Nerem RM. Endothelial cellular response to altered shear stress. *American Journal of Physiology-Lung Cellular and Molecular Physiology* 2001; 281(3): L529–L533.

5 | APPENDIX

5.1 | Proof of Property 1 in 3.2.1 for pure convection

Assuming $U_i^n \geq 0 \quad \forall i$, let us show that $U_i^{n+1} \geq 0 \, \forall i$. Equations (18) and (26) can be written as:

$$\begin{cases} U_i^{n+1} = a + b - d \\ \quad a = C_i^n V_i (1 - \Delta t \dfrac{Q_i}{V_i}) + \displaystyle\sum_{j \in \Gamma^-(i)} C_j^n Q_{j,i} \Delta t \\ \quad b = \dfrac{\Delta t}{2} \displaystyle\sum_{j \in \Gamma^-(i)} (1 - \Delta t \dfrac{Q_{j,i}}{V_j}) \dfrac{Q_{j,i}}{Q_j} \displaystyle\sum_{p \in \Gamma^-(j)} Q_{p,j} \Phi(r_-) \\ \qquad\qquad (C_i^n - C_j^n) \\ \quad c = \dfrac{\Delta t}{2} \displaystyle\sum_{j \in \Gamma^-(i)} \dfrac{Q_{j,i}}{Q_i} \displaystyle\sum_{l \in \Gamma^+(i)} (1 - \Delta t \dfrac{Q_{i,l}}{V_i}) Q_{i,l} \Phi(r_+) \\ \qquad\qquad (C_l^n - C_i^n) \\ r_- = \dfrac{C_j^n - C_p^n}{C_i^n - C_j^n} \\ r_+ = \dfrac{C_i^n - C_j^n}{C_l^n - C_i^n} \end{cases} \tag{36}$$

Let us split b, d such as :

$$\begin{cases} b = B_1 + B_2 + B_3 \\ B_1 = \dfrac{\Delta t}{2} \displaystyle\sum_{j \in \Gamma^-(i) | C_i^n \geq C_j^n} (1 - \Delta t \dfrac{Q_{j,i}}{V_j}) \dfrac{Q_{j,i}}{Q_j} \\ \qquad \displaystyle\sum_{p \in \Gamma^-(j)} Q_{p,j} \Phi(r_-)(C_i^n - C_j^n) \\ B_2 = \dfrac{\Delta t}{2} \displaystyle\sum_{j \in \Gamma^-(i) | C_i^n < C_j^n} (1 - \Delta t \dfrac{Q_{j,i}}{V_j}) \dfrac{Q_{j,i}}{Q_j} \\ \qquad \displaystyle\sum_{p \in \Gamma^-(j) | C_j^n \geq C_p^n} \Phi(r_-) Q_{p,j} (C_i^n - C_j^n) \\ B_3 = \dfrac{\Delta t}{2} \displaystyle\sum_{j \in \Gamma^-(i) | C_i^n < C_j^n} (1 - \Delta t \dfrac{Q_{j,i}}{V_j}) \dfrac{Q_{j,i}}{Q_j} \\ \qquad \displaystyle\sum_{p \in \Gamma^-(j) | C_j^n < C_p^n} \Phi(r_-) Q_{p,j} (C_i^n - C_j^n) \end{cases} \tag{37}$$

and

$$\begin{cases} d = D_1 + D_2 + D_3 \\ D_1 = \dfrac{\Delta t}{2} \displaystyle\sum_{l \in \Gamma^+(i) | C_i^n \geq C_l^n} (1 - \Delta t \dfrac{Q_{i,l}}{V_i}) Q_{i,l} \\ \qquad \displaystyle\sum_{j \in \Gamma^-(i)} \Phi(r_+) \dfrac{Q_{j,i}}{Q_i} (C_l^n - C_i^n) \\ D_2 = \dfrac{\Delta t}{2} \displaystyle\sum_{l \in \Gamma^+(i) | C_i^n < C_l^n} (1 - \Delta t \dfrac{Q_{i,l}}{V_i}) Q_{i,l} \\ \qquad \displaystyle\sum_{j \in \Gamma^-(i) | C_i^n \leq C_j^n} \Phi(r_+) \dfrac{Q_{j,i}}{Q_i} (C_l^n - C_i^n) \\ D_3 = \dfrac{\Delta t}{2} \displaystyle\sum_{l \in \Gamma^+(i) | C_i^n < C_l^n} (1 - \Delta t \dfrac{Q_{i,l}}{V_i}) Q_{i,l} \\ \qquad \displaystyle\sum_{j \in \Gamma^-(i) | C_i^n > C_j^n} \Phi(r_+) \dfrac{Q_{j,i}}{Q_i} (C_l^n - C_i^n) \end{cases} \tag{38}$$

It can be directly seen that:

$$\begin{aligned}
&\bullet\ C_j^n \le C_i^n \Rightarrow B_1 \ge 0 \quad \forall p \in \Gamma^-(j) \text{ as } \Phi(r_-) \ge 0\\
&\bullet\ C_j^n \ge C_p^n \text{ and } C_i^n < C_j^n \Rightarrow r_- \le 0 \Rightarrow \Phi(r_-) = 0 \Rightarrow B_2 = 0\\
&\bullet\ C_i^n \ge C_l^n \Rightarrow D_1 \le 0 \quad \forall j \in \Gamma^-(i)\\
&\bullet\ C_i^n < C_l^n \text{ and } C_i^n \le C_j^n \Rightarrow r_+ \le 0 \Rightarrow \Phi(r_+) = 0 \Rightarrow D_2 = 0
\end{aligned} \tag{39}$$

Therefore equation (36) becomes:

$$\begin{aligned}
U_i^{n+1} &= a + \overbrace{B_1}^{\ge 0} + B_3 - \overbrace{C_1}^{\le 0} - D_3\\
&= A_1 + A_2 + A_3 + \overbrace{B_1}^{\ge 0} + B_3 - \overbrace{C_1}^{\le 0} - D_3
\end{aligned} \tag{40}$$

with

$$\begin{cases}
A_1 = -\sum\limits_{j\in\Gamma^-(i)|C_i^n<C_j^n} (C_i^n - C_j^n) Q_{j,i}\Delta t\\
A_2 = \sum\limits_{j\in\Gamma^-(i)|C_i^n=C_j^n} (C_i^n - C_j^n)\Delta t Q_{j,i} \quad (\to 0)\\
A_3 = -\sum\limits_{j\in\Gamma^-(i)|C_i^n>C_j^n} (C_i^n - C_j^n) Q_{j,i}\Delta t + C_i^n V_i
\end{cases} \tag{41}$$

Let us now show that:

1. ♣ : $A_1 + B_3 \ge 0$ under equation (20)
2. ♠ : $A_3 - C_3 \ge 0$ under detailed conditions

♣ :

$$\begin{aligned}
A_1 + B_3 &= \sum_{j\in\Gamma^-(i)|C_i^n<C_j^n} (C_i^n - C_j^n)\frac{\Delta t}{2} Q_{j,i} K\\
K &= -2 + (1 - \Delta t \frac{Q_{j,i}}{V_j}) \sum_{p\in\Gamma^-(j)|C_j^n<C_p^n} \frac{Q_{p,j}}{Q_j}\Phi(r_-)
\end{aligned} \tag{42}$$

In case of

- a MinMod limiter: $\Phi(r_-) = \max(0, \min(1, r_-)) \le 1$
- a MC limiter: $\Phi(r_-) = \max(0, \min(2r_-, 2, \frac{1+r_-}{2})) \le 2$
- a Superbee limiter: $\Phi(r_-) = \max(0, \min(2r_-, 1), \min(r_-, 2)) \le 2$
- a VanLeer limiter: $\Phi(r_-) = \frac{r_- + |r_-|}{1+r_-} \le 2$

Let us prove that $K \le 0$ for the worst case attained if $\Phi(r_-) = 2$, by equation (20) and as $(1 - \Delta t \frac{Q_{j,i}}{V_j}) \ge 0$. We have:

$$\begin{aligned}
K &= -2 + (1 - \Delta t \frac{Q_{j,i}}{V_j})\lambda_{p,j} 2\\
0 \le \lambda_{p,j} &= \sum_{p\in\Gamma^-(j)|C_j^n<C_p^n} \frac{Q_{p,j}}{Q_j} \le 1\\
K &= \underbrace{2(\lambda_{p,j} - 1)}_{\le 0} - \underbrace{\Delta t \frac{Q_{j,i}}{V_j}\lambda_{p,j} 2}_{\ge 0}
\end{aligned} \tag{43}$$

Hence, $K \le 0$ and $C_i^n < C_j^n \Rightarrow A_1 + B_3 \ge 0$ under equation (20).

♠ :

$$\begin{aligned}
A_3 - D_3 = &\sum_{j\in\Gamma^-(i)|C_i^n>C_j^n} (C_j^n - C_i^n)\frac{\Delta t}{2} Q_{j,i} L\\
&+ \underbrace{\sum_{j\in\Gamma^-(i)|C_i^n>C_j^n} C_j^n Q_{j,i}\frac{V_i}{Q_i}}_{\ge 0}\\
&+ \underbrace{\sum_{j\in\Gamma^-(i)|C_i^n\le C_j^n} \frac{Q_{j,i}}{Q_i} C_i^n V_i}_{\ge 0}\\
L = &2 - \frac{2V_i}{Q_i\Delta t} + \sum_{l\in\Gamma^+(i)|C_i^n<C_l^n} (1 - \Delta t \frac{Q_{i,l}}{V_i})\frac{Q_{i,l}}{Q_i}\Phi(r_+)\frac{1}{r_+}
\end{aligned} \tag{44}$$

Similarly to what has been done in ♣: In case of

- a MinMod limiter: $\frac{\Phi(r_+)}{r_+} = \frac{\max(\min(1, r_+), 0)}{r_+} \le 1$
- a MC limiter: $\frac{\Phi(r_+)}{r_+} = \frac{\max(0, \min(2r_+, 2, \frac{1+r_+}{2}))}{r_+} \le 2$
- a Superbee limiter: $\frac{\Phi(r_+)}{r_+} = \frac{\max(0, \min(2r_+, 1), \min(r_+, 2))}{r_+} \le 2$
- a VanLeer limiter: $\frac{\Phi(r_+)}{r_+} = \frac{r_+ + |r_+|}{r_+(1+r_+)} \le 2$

Let us prove that $L \le 0$ under certain conditions. As by equation (20) $(1 - \Delta t \frac{Q_{i,l}}{V_i}) \ge 0$, the worst case is therefore attained if $\frac{\Phi(r_+)}{r_+} = 2$ where we have:

$$L = 2(1 - \frac{V_i}{Q_i\Delta t} + \sum_{l\in\Gamma^-(i)|C_i^n<C_l^n} (1 - \Delta t \frac{Q_{i,l}}{V_i})\frac{Q_{i,l}}{Q_i}) \tag{45}$$

$$L \le 0 \Rightarrow \frac{V_i}{Q_i\Delta t} \ge 1 + \sum_{l\in\Gamma^-(i)|C_i^n<C_l^n} (1 - \Delta t \frac{Q_{i,l}}{V_i})\frac{Q_{i,l}}{Q_i} \tag{46}$$

that gives the second condition as $L \le 0 \Rightarrow A_3 - D_3 \ge 0$.

Therefore, the numerical scheme based on (26) is positivity preserving under (20) and (46).

FIGURE 9 (A) Evolution of the blood apparent viscosity as a function of the radius of the tube and the discharge hematocrit value. It highlights the high nonlinearity of this function with the radius. (B) Fractional blood flows and hematocrit flows in a bifurcation of mother branch diameter $d = 7.5\mu m$ and daughter branches diameters of $6\mu m$ (d1) and $8\mu m$ (d2) in case of no plasma skimming, with the linear law considering $M = 5.25$, and the nonlinear law. The dots represent experimental data from [19] while dashed lines correspond to the considered law defined in section 2.2.

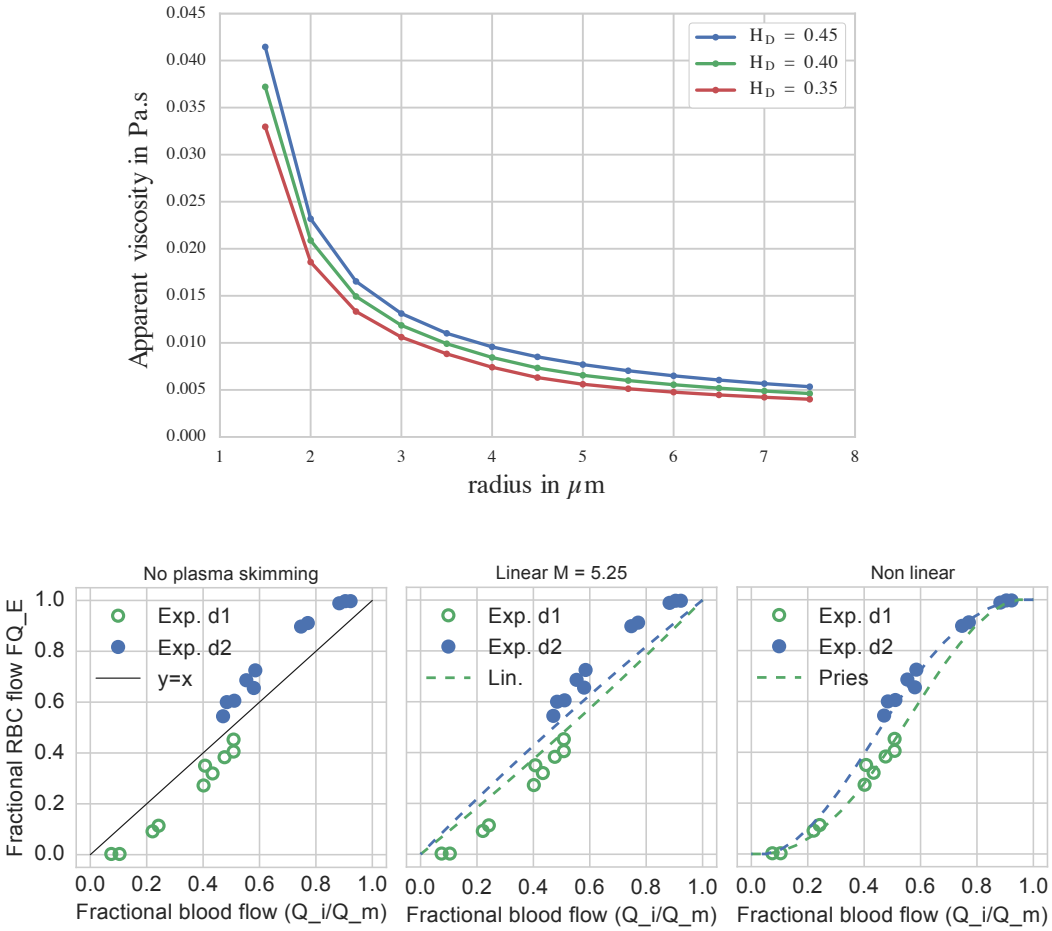

6 | SUPPLEMENTARY INFORMATION

6.1 | Erythrocytes effects on apparent viscosity

To account for the effect of erythrocytes on blood apparent viscosity, the Fahraeus-Linqvist effect, Pries and Secomb [14] proposed an empirical law that links the vessel radius $r_{i,j}$ and discharge hematocrit $H_D(i,j)$ to the blood apparent viscosity and is referred to as $W(r_{i,j}, H_D(i,j), \eta_{plasma})$:

$$\eta_{i,j} = \eta_{plasma}\left[1 + (\eta_{45} - 1)\frac{(1 - H_D(i,j))^C - 1}{(1 - 0.45)^C - 1}\left(\frac{2r_{i,j}}{2r_{i,j} - 1.1}\right)^2\right]\left(\frac{2r_{i,j}}{2r_{i,j} - 1.1}\right)^2 \quad \forall (i,j) \in E \tag{47}$$

with

$$\begin{aligned} C &= (0.8 + e^{-0.15r_{i,j}})(-1 + (1 + 10^{-11}(2r_{i,j})^{12}))^{-1}) + (1 + 10^{-11}(2r_{i,j})^{12}))^{-1}; \\ \eta_{45} &= 6e^{-0.17r_{i,j}} + 3.2 - 2.44e^{-0.06(2r_{i,j})^{0.645}} \end{aligned} \tag{48}$$

This effect can be seen in figure 9(A) when varying the radius for several discharge hematocrit values.

FIGURE 10 Hemodynamics patterns obtained on a 2D axial cut liver lobule with constant radius for pressure (first row), flow (second row) in log scale and discharge hematocrit (third row), without plasma skimming (left column), with plasma skimming considering the nonlinear law linear (middle column) and the linear law. The absolute difference to the case without plasma skimming for each law is plotted in the two last columns for each criteria (pressure, flow and discharge hematocrit). Note the significant difference between nonlinear law and absence of plasma skimming (last row, last but one column), while for all other cases differences are negligible.

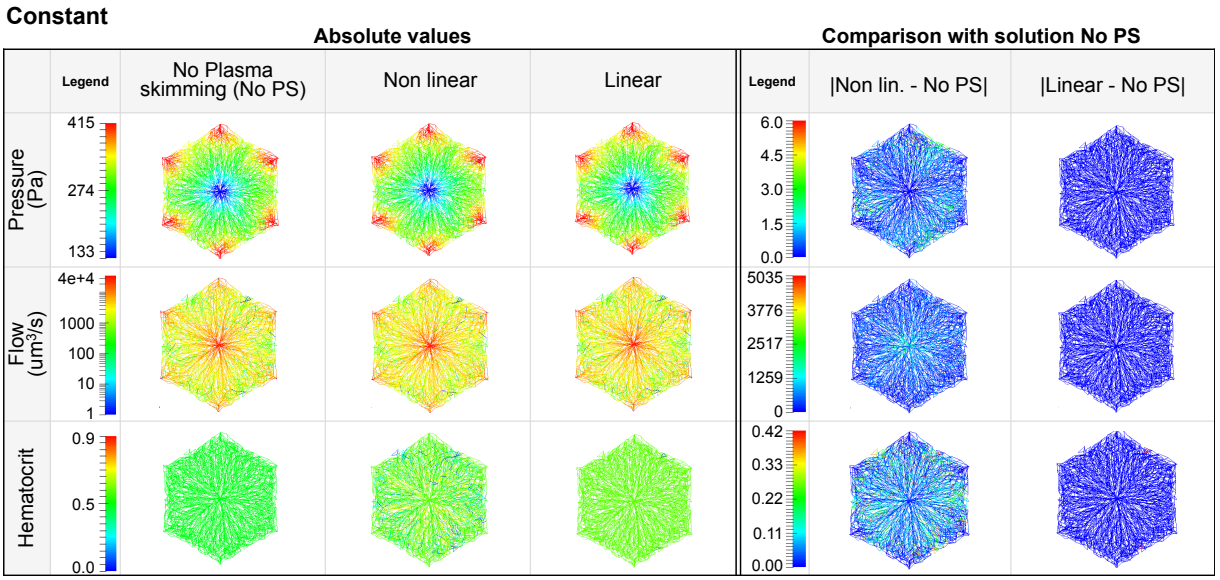

6.2 | Description of hemodynamic results

Hemodynamics patterns

The detailed hemodynamics patterns for each liver lobule representative network are presented in figures 10, 11 and 12. The median changes introduced by the nonlinear law are higher compared to the linear one (figure 14). Finally, the hematocrit distribution is detailed in figure 13 in each case: no plasma skimming, with the linear and nonlinear laws. It highlights that introducing plasma skimming leads to a wider distribution of hematocrit, with a mean lower than $H_D = 0.442$, the value set when no plasma skimming is considered.

Wall-shear stress

A common indicator looked at when simulating blood flow is wall shear stress. In case of Poiseuille flow, it is computed as:

$$\tau_{i,j} = \frac{4\eta Q_{i,j}}{\pi r_{i,j}^3} \quad \forall (i,j) \in E \tag{49}$$

In an organ, a high wall shear stress induces injuries of the endothelium, hence the organs tend to reduce the wall shear stress [83,51]. This reduction can also be a criteria to validate a model as in [84,85]. Wall shear stress is also studied when too low to better understand the influence of a disease on the endothelium, for example in case of atherosclerosis [86], or focusing on the response of the endothelium to a shear stress alteration [87]. Figure 15 details the patterns obtained for the three considered geometries and for the two studied plasma skimming laws. This pattern is homogeneous through the liver lobule, with similar values in the healthy (HLL) and dilated peri-central area (DLL), when the radii are drawn from a Gaussian distribution, while the values are higher if the radii are constant all over the lobule (CLL). The highest values are located along the main flow pathways, which is expected looking at equation (49). Yet, for the lobule with a wider CV, the peri-central zone presents lower wall shear stress values. This indicates that for such a type of injuries in the liver, the endothelial cells should not be damaged, but rather flow and metabolism might be affected. Independently of the studied plasma skimming law, the differences to the case without plasma skimming are very low, similarly to the case of the pressure.

FIGURE 11 Hemodynamics patterns obtained in a 2D axial cut healthy liver lobule with radii drawn from a Gaussian distribution for pressure (first row), flow (second row), discharge hematocrit (third row) without plasma skimming (left column), with plasma skimming considering the nonlinear law linear (middle column) and the linear law (right column). The absolute difference to the case without plasma skimming for each law is plotted in the two last columns for each criteria (pressure, flow and discharge hematocrit). Note the significant difference between nonlinear law and absence of plasma skimming (last row, last but one column), while for all other cases differences are negligible.

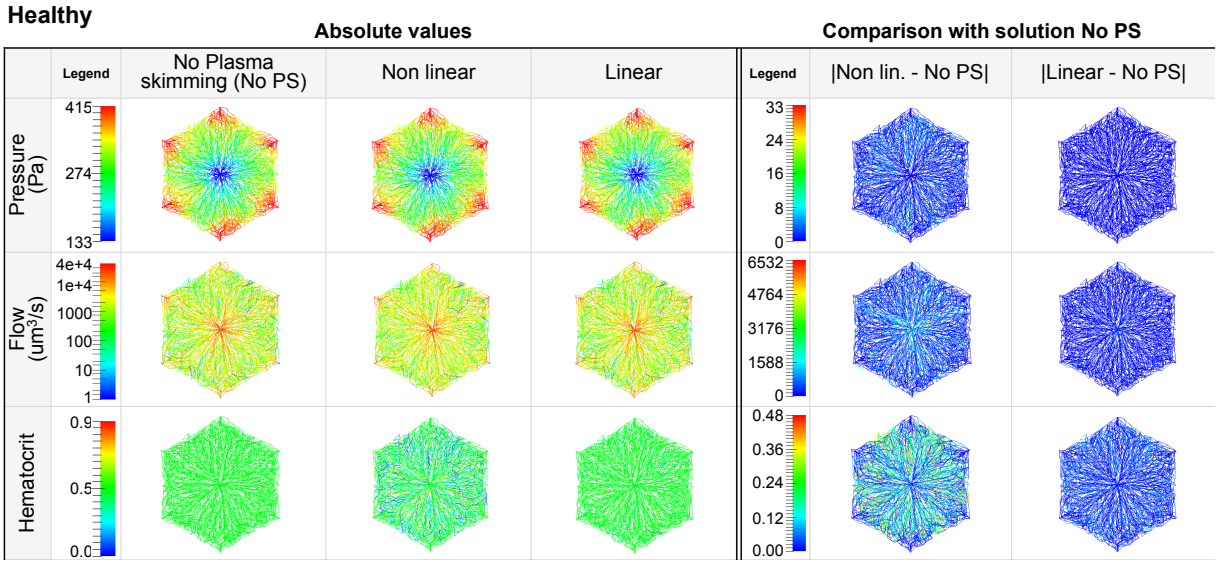

6.3 | Analytic convection-reaction solutions in single tubes

In one cylindrical tube of constant radius, the analytic solution for the concentration at a node i $c_i(t)$ is given by the characteristics' method, i.e. for convection without reaction:

$$c(x,t) = g\left(t - \frac{x}{v}\right) \tag{50}$$

with $g(t)$ the input concentration function (a Gaussian $N = (7.5, 2.25)$), and if $t - \frac{x}{v} > 0$ with v the blood velocity set to $138.8 \mu m.s^{-1}$. Here, we consider an analytical solution discretized in space that becomes:

$$c_i(t) = g\left(t - \sum_{j=0}^{i-1} \frac{L_j}{v}\right) \quad \forall i \in N \tag{51}$$

if $t - \sum_{j=0}^{i-1} \frac{L_j}{v} > 0$. At a converging intersection,(i.e. several upstream branches connecting into a single downstream branch) the average concentration weighted by the blood flow in each upstream branch is taken as the resulting value in the downstream branch:

$$c_i(t) = \sum_{j \in \Gamma^-(i)} c_j(t - \frac{L_{j,i}}{v_{j,i}}) \frac{Q_{j,i}}{Q_i} \quad \forall i \in N \tag{52}$$

At diverging intersections (i.e. one upstream branch connected to several downstream branches) and the resulting concentration in downstream branches of a multi-furcations has to be defined. In this work, we choose to ensure concentration continuity:

$$\forall j \in \Gamma^+(i) \quad c_j(t) = c_i(t - \frac{L_{i,j}}{v_{i,j}}) \quad \forall i \in N \tag{53}$$

When a convection-reaction equation is considered, analytic solutions can be defined, here for a tube, for the linear regime of equation (13):

$$c(x,t) = g\left(t - \frac{x}{v}\right) e^{-\frac{v_{r,max}}{K_{r,m}} \cdot \frac{x}{v}} \tag{54}$$

and for a saturated regime, equation (14):

$$c(x,t) = g\left(t - \frac{x}{v}\right) - \frac{v_{r,max}}{K_{r,m}} x \tag{55}$$

However, no analytical solution exists for convection coupled to a nonlinear Michaelis-Menten reaction term.

FIGURE 12 Hemodynamics patterns obtained in a 2D axial cut of a liver lobule with a dilated peri-central zone for pressure (first row), flow (second row), discharge hematocrit (third row) without plasma skimming (left column), with plasma skimming considering the nonlinear law linear (middle column) and the linear law (right column). The absolute difference to the case without plasma skimming for each law is plotted in the two last columns for each criteria (pressure, flow and discharge hematocrit). Note the significant difference between nonlinear law and absence of plasma skimming (last row, last but one column), while for all other cases differences are negligible.

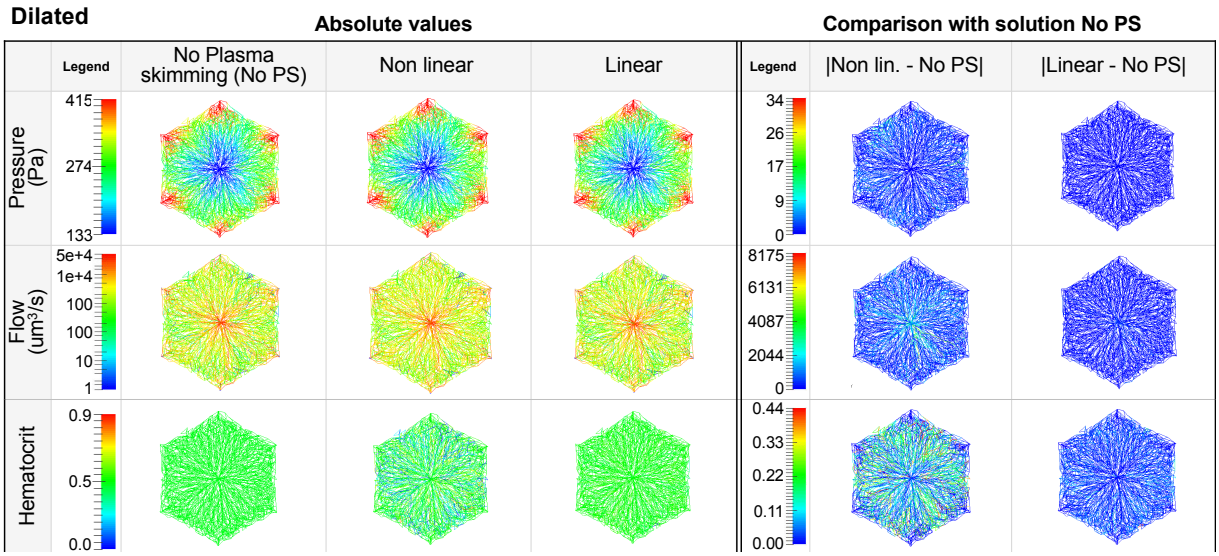

FIGURE 13 Discharge hematocrit distribution for a liver lobule with constant radius (first row), for a healthy liver lobule (second row) and for a liver lobule with dilated capillaries (third row). The probability density distribution of each hemodynamics component without including plasma skimming (red distributions), with a linear plasma skimming (green) and a nonlinear plasma skimming (blue) law are plotted.

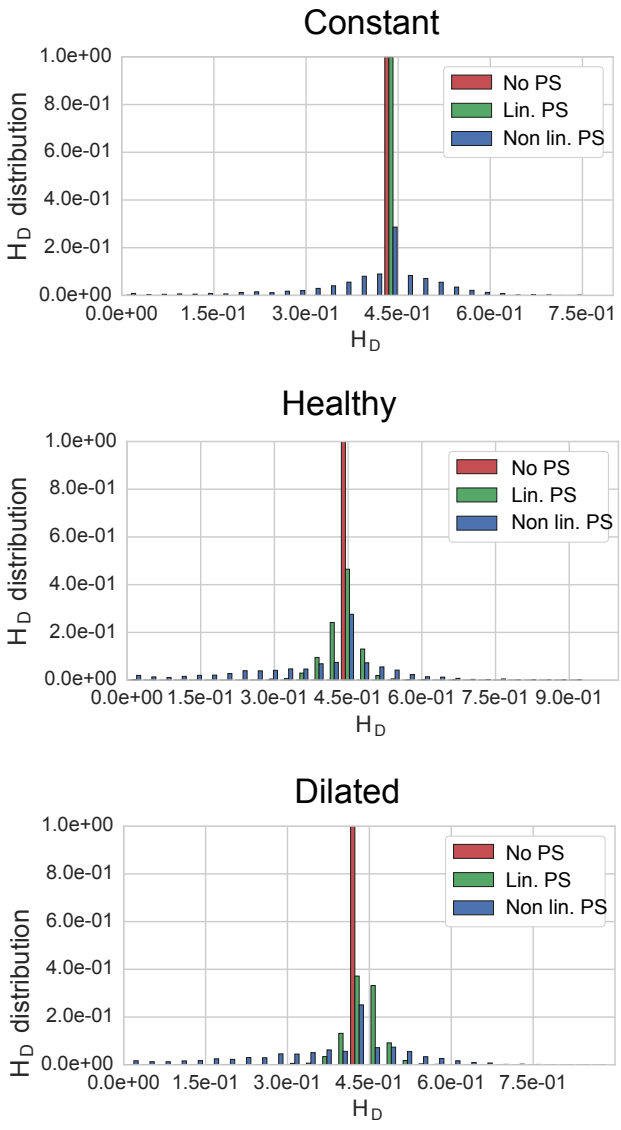

FIGURE 14 Median flow (full bars) and discharge hematocrit (dashed bars) relative difference when plasma skimming is included to the case without plasma skimming for three geometries: Constant, Healthy and Dilated. For the linear law in the constant geometry, the median difference to the baseline solution is barely seen as it is extremely close to zero. Independently of the geometry, the nonlinear law predicts hemodynamics patterns different from the case without plasma skimming whereas the linear law leads to patterns close to the case without plasma skimming.

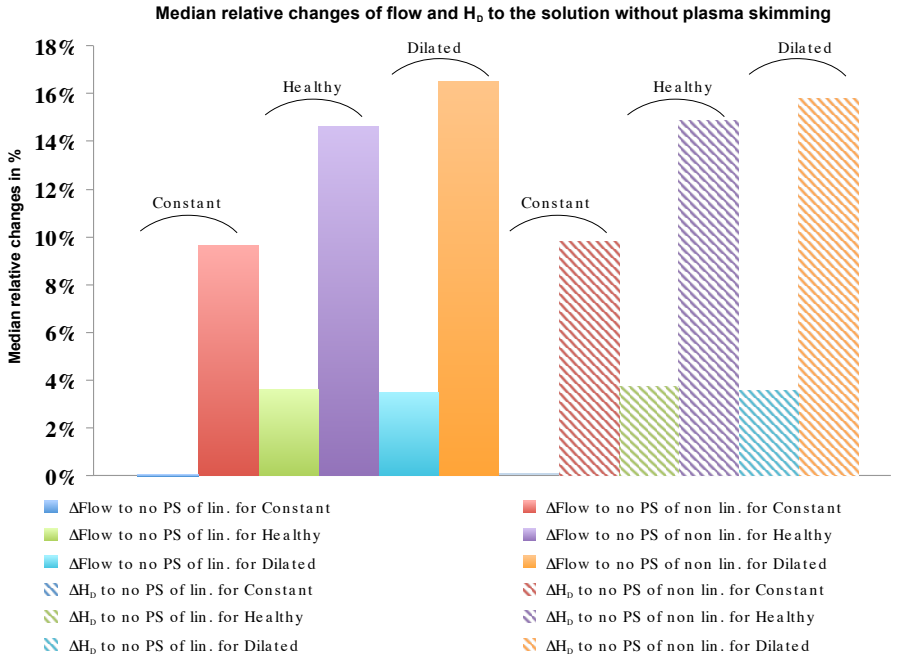

FIGURE 15 Wall shear stress patterns for each one of the three lobule geometries: constant radius (top row), radius drawn from a Gaussian distribution (middle row), wider CV (bottom row) and in case of no plasma skimming (left column), in case of Pries nonlinear plasma skimming law (middle column) and Gould & Linninger linear plasma skimming law (right column) in Pa.